Molecular Modulator Approach for Controlling the Length of Chiral 1D Single-Helical Gold Nanoparticle Superstructures

by

Yuyu Zhang

B.A, Earlham College, 2020

Submitted to the Graduate Faculty of the

Dietrich School of Arts and Sciences in partial fulfillment

of the requirements for the degree of

Master of Science

University of Pittsburgh

2023

UNIVERSITY OF PITTSBURGH

DIETRICH SCHOOL OF ARTS AND SCIENCES

This thesis was presented

by

Yuyu Zhang

It was defended on

June 9, 2022

and approved by

Dr. Jill Millstone, Leo B. and Teresa Y. Wegemer Endowed Chair of Professor, Department of Chemistry

Dr. W. Seth Childers, Associate Professor, Department of Chemistry

Dr. Nathaniel L. Rosi, Covestro Endowed Chair of Chemistry, Department of Chemistry

Thesis Advisor Director: Dr. Nathaniel Rosi, Covestro Endowed Chair of Professor, Department of Chemistry

Molecular Modulator Approach for Controlling the Length of Chiral 1D Single-Helical Gold Nanoparticle Superstructures

Yuyu Zhang, MS

University of Pittsburgh, 2023

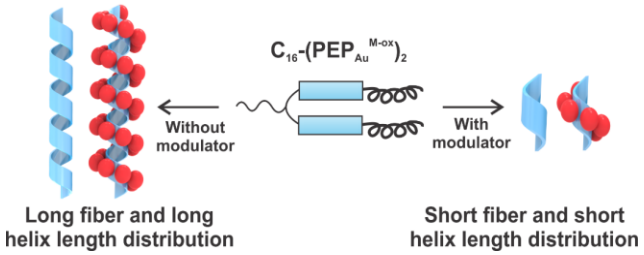

Figure 1. Abstract figure

Peptide-based methods have proven useful for constructing helical gold nanoparticle superstructures that exhibit strong plasmonic chiroptical activity. Superstructure syntheses using the amphiphilic peptide conjugate C_{16}-(AYSSGAPPM^{ox}PPF)$_2$ typically yield 1D helices with a broad length distribution. In this study, we introduce a molecular modulator approach for controlling helix length. It represents a first step toward achieving narrowly disperse populations of single helices fabricated using peptide-based methods. Varying amounts of modulator, C_{16}-(AYSSGA)$_2$, were added to C_{16}-(AYSSGAPPM^{ox}PPF)$_2$-based single-helix syntheses, resulting in decreased helix length and narrowing of the helix length distribution. Kinetic studies of fiber assembly were performed to investigate the mechanism by which the modulator affects helix length. It was found that the modulator leads to rapid peptide conjugate nucleation and fiber growth, which in turn results in large amounts of short fibers that serve as the underlying scaffold for the single-helix superstructures. These results constitute important advances toward generating monodisperse samples of plasmonic helical colloids.

Table of Contents

List of Tables

List of Figures

1.0 Introduction

In nature, molecules such as lipids and proteins can be precisely spatially arranged to construct structurally-intricate and functionally-sophisticated nanostructures. Various biological structures, such as bones, teeth, shells, are formed via self-assembly coupled with the process of biomineralization[1–4]. Inspired by nature, chemists have developed a robust and versatile collection of synthetic biopolymers to direct the formation of complex nanostructures[5–10]. Individual molecular building blocks encoded with desired chemical information and functionality can spontaneously organize into hierarchical assemblies. Furthermore, synthetic biopolymers can be designed to encode metal-binding functionality and thus can direct the synthesis and assembly of inorganic nanoparticles[11–16]. The resulting nanoparticle superstructures can exhibit emergent novel properties and can potentially be used for wide-ranging applications[14–18].

Nanoparticles (NPs) (< 100 nm in one dimension) have large surface area-to-volume ratios and exhibit unique optical, electrical, physical, and chemical properties[19]. When NPs couple together to form higher order assemblies, they exhibit properties distinct from the individual components[12,13]. However, it is typically challenging to precisely direct the spatial assembly of nanoparticles without using some sort of scaffold[15,16]. Biopolymers such as DNA origami and peptide amphiphiles have proven to be successful candidates for directing NP assembly, owing to their tunability and ability to bind NPs[12–16]. A diverse array of 1D NP assemblies, such as chiral helical assemblies, 1-dimensional linear assemblies, and pyramidal assemblies have been successfully prepared[12,13]. 1-D NP assemblies can play critical roles in improving efficiencies and realizing the miniaturization of various electronic or optoelectronic devices[15].

Peptides exhibit distinct advantages for assembling NPs into NP superstructures compared to their rich diversity of amino acid sequences, highly modular assembly, and NP-recognition capabilities[20–22]. The Rosi group has developed peptide-based NP assembly methods, where highly programmable and rationally designed peptide conjugate (PC) molecules are used to direct the nucleation and synthesis as well as the spatial arrangements of NPs[23]. This unique one-pot synthetic method integrates peptide self-assembly and peptide-based biomineralization of nanoparticles into one simultaneous process[23]. The PCs consist of a peptide head group which recognizes and binds specific inorganic surfaces (e.g., biomineralization peptides isolated via phage display[24–26]) covalently attached to an organic self-associating moiety. In the presence of inorganic salts and reducing agents, these sophisticated constructs bind onto the nucleating NPs and direct their assembly into a diverse array of well-defined superstructures such as chiral helical assemblies (e.g double[23,27]-, and single-helical assemblies[28]), spheres[29], and 1-dimensional assemblies[30,31]. Previous efforts have led to deliberate modulation chiroptical properties within a specific class of peptide-directed chiral helical NP assemblies via control over helicity (e.g., double or single)[32], helical pitch[33], particle dimensions[34], and helix handedness[27]. However, the current approach for constructing the 1D chiral single-helical NP assemblies does not offer control over helix length. Helix length is an important parameter to consider for future applications such as reducing electron transfer losses, increasing optical device efficiencies, and facilitating incorporation with other materials (e.g. polymers) to form functional composite materials. In this thesis, I present a molecular modulator approach for controlling the length of these single-helical assemblies. The described methods are used to prepare samples of single helices with defined lengths and strong plasmonic chiroptical activity. These methods could be broadly applicable for controlling the length of supramolecular polymers, in general.

2.0 Molecular Modulator Approach for Controlling the Length of Chiral 1D Single-Helical Gold Nanoparticle Superstructures

2.1 Introduction

1D nanoparticle (NP) assemblies have attracted broad interest due to proposed applications that derive from their ensemble plasmonic properties and their ability to directionally transport light and electrons. [15,35,36] The properties of these assemblies depend on factors such as NP size, shape, composition, interparticle distances, and also the 3D organization of component NPs along the axis of the 1D assembly. For example, 1D helical NP assemblies[37] give rise to unique plasmonic chiroptical behavior which renders them potentially promising components of a variety optical metamaterials.[13,38] From a practical point of view, it is important to be able to control the length of these superstructures. For example, those with short, well-defined lengths may experience reduced losses during directional light or electron transfer. Furthermore, fabrication of monodisperse 1D superstructures may facilitate their processing and integration into other materials and devices.

Most 1D NP superstructures are prepared using template-based approaches.[12,14–16,35–37] A wide variety of templates have been explored, from microorganisms to polymers to supramolecular fibers. In the latter case, molecular building blocks assemble to form 1D fibers which serve as scaffolds for organizing NPs. A distinct advantage of this approach is its molecular tunability, allowing for molecular-level control of the structure and properties of the NP superstructure. As an example, we have developed programmable peptide-based methods for assembling a wide variety of NP superstructures, including spherical architecture,[29,39,40] 1D chains,[30,41] and a diverse

collection of chiral 1D helices.[23,27,32,42,43] The basis of the methodology are peptide conjugate molecules that both bind to NPs and direct their assembly. They are designed to assemble into a soft template that serves as the underlying scaffold for arranging NPs. We have demonstrated how molecular modifications to the peptide conjugate translate into discernible and consequential changes in the morphology, structural metrics, and collective plasmonic properties of the NP superstructure.[27,31–34,39,44] In the case of chiral helical gold (Au) NP superstructures, we have shown how the composition of the peptide conjugate can be tuned to control the degree of helicity (e.g., double or single),[23,28] helical pitch,[31,33] particle dimensions[34], and helix handedness (left or right).[27] However, we have yet to achieve helix length control. Our reported syntheses typically yield long helices (>1 μm) with broad length distributions (Appendix Figure 3 and 4). Helix length is an important parameter to control, especially when considering potential downstream applications that may require monodisperse populations of helices of a specific length. To address this challenge, we present here a molecular modulator approach for preparing Au NP single helices with controllable length and narrow length distributions. We show that superstructure length can be tuned by adjusting the amount of molecular modulator added to the syntheses. Importantly, the resultant relatively monodisperse samples of Au NP single helices maintain strong plasmonic chiroptical activity.

2.2 Results and Discussion

Controlling the length of 1-D NP superstructures fabricated using soft template approaches requires control over the length of the template itself. Both physical and chemical approaches have

been used to control template length. Physical approaches include ultrasonication[45–47] and extrusion,[48] but they are not particularly well-suited for controlling the length of an NP superstructure because they may disrupt or destroy the organization of NPs. Chemical approaches commonly involve the design of molecular additives that act as i) "caps" to halt polymerization;[49–52] ii) "initiators" for controlling fiber nucleation;[53–56] or iii) agents that disassemble the pre-assembled template.[57,58] Motivated to control the length of our single-helical Au NP superstructures, we drew inspiration from these prior studies and set forth to design peptide-based molecular modulators for controlling the length of the peptide fibers underlying the Au NP single helices.

Our single-helical Au NP superstructures (Figure 2a) are prepared using a 'divalent' peptide conjugate consisting of two $PEP_{Au}^{M\text{-}ox}$ (AYSSGAPPM^{ox}PPF; M^{ox} indicates methionine sulfoxide) head groups attached at their N-termini to an aliphatic tail (*e.g.*, C_{16}-C_{22}) (Figure 2b).[28,33] These peptide conjugates assemble into 1D helical ribbons in aqueous buffers (Figure 2c). Through various microscopy, spectroscopy, and diffraction studies, we determined that these helical ribbons consist of a monolayer of C_x-$(PEP_{Au}^{M\text{-}ox})_2$ arranged orthogonally to their surface (Figure 2c).[28] C_x-$(PEP_{Au}^{M\text{-}ox})_2$ can be divided into an "assembly module" and a "particle binding module" (Figure 2b).[21] Within the context of the 1D helical ribbon fibers, the C-terminus of $PEP_{Au}^{M\text{-}ox}$, PPM^{ox}PPF, is exposed on the outer surface of the ribbon, exhibits PPII secondary structure, and serves as the "particle binding module". The N-terminal amino acids, AYSSGA, coupled with the aliphatic tail comprise the "assembly module": AYSSGA engages in β-sheet formation and the aliphatic tails promote aggregation in aqueous media. This assembly serves as a basis for designing a molecular modulator for controlling fiber length.

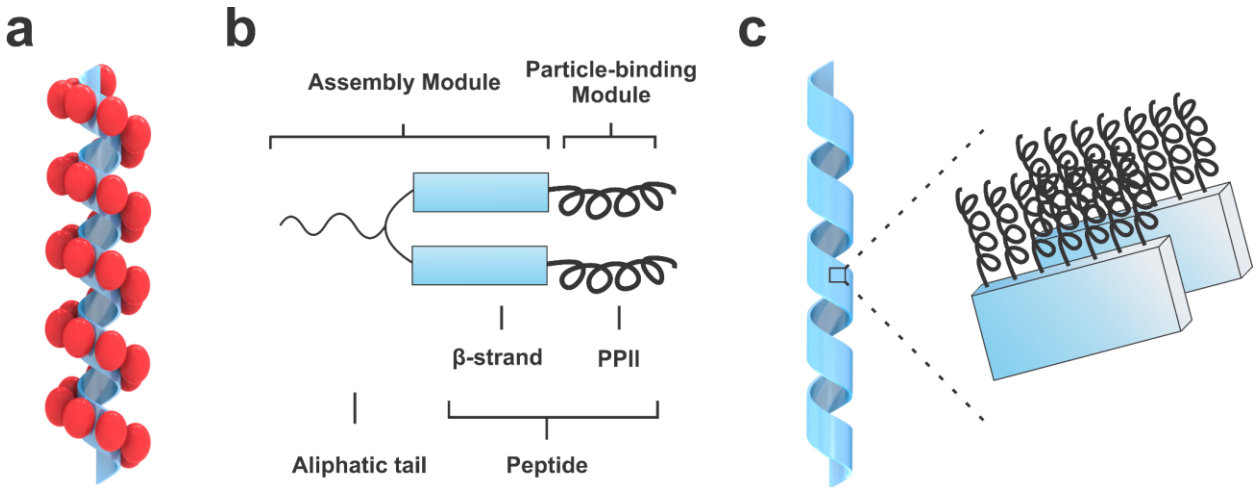

Figure 2.Assembly of Au NP single helices. a) Cartoon representation of single helices in which the Au NPs decorate the external face of helical ribbons assembled from C_x-$(PEP_{Au}{}^{M\text{-}ox})_2$. b) C_x-$(PEP_{Au}{}^{M\text{-}ox})_2$ conjugate (x = 16-22, $PEP_{Au}{}^{M\text{-}ox}$ = AYSSGAPPM^{ox}PPF) consists of two modules: C_x-AYSSGA is the assembly module and the C-terminus, PPM^{ox}PPF, is the particle-binding module. c) Helical ribbon assembly model: monolayers of C_x-$(PEP_{Au}{}^{M\text{-}ox})_2$ arrange orthogonal to the ribbon surface. The ribbon thickness is approximately equal to the extended length of the peptide. The hydrogen bonding between the β-strands is along the long axis of the ribbons and intersheet stacking occurs along the axis perpendicular. The aliphatic tails (not shown) likely aggregate on the inner surface of the ribbon.

Using single helices prepared with C_{16}-$(PEP_{Au}{}^{M\text{-}ox})_2$ (Appendix Figures 1a and 2a) as the basis for this study, we designed a modulator, C_{16}-$(AYSSGA)_2$ (Appendix Figure 1b and 2b), which is sequence-matched to the C_{16}-$(PEP_{Au}{}^{M\text{-}ox})_2$ β-sheet region and contains only its 'assembly module' components. Based on our assembly model, we postulated that C_{16}-$(AYSSGA)_2$ would readily form fibers but would not bind to Au NPs or direct their assembly, because it lacks the particle- binding module. We designed a set of experiments in which incremental amounts of modulator were added to single-helix syntheses to examine the effect of modulator on helix length. The single- helix products were analyzed using transmission electron microscopy (TEM). In brief, each synthesis was repeated to ensure reproducibility and at least 30 TEM images of product were collected for each synthetic replicate. The lengths of the helices within these images were

measured, and the average helix length and helix length distribution were calculated for each synthetic condition.

We first prepared Au NP single helices using C_{16}-$(PEP_{Au}^{M\text{-}ox})_2$ by following our previously reported synthetic procedure (Appendix Figure 3).[28] Based on measuring 260 helical superstructures, helix lengths ranged from ~80 to 25,000 nm, with a median length of 693 nm and an average length of ~1740 nm. ~40% of the helices were longer than 1000 nm and ~3% were longer than 10,000 nm (Appendix Figure 4). We concluded from these results that unmodulated syntheses yield a broad distribution of helix lengths.

We next studied the assembly of C_{16}-$(AYSSGA)_2$ and determined whether it could direct NP assembly. C_{16}-$(AYSSGA)_2$ was incubated in aqueous buffer overnight and the resulting assemblies were then imaged using TEM. Negatively stained TEM images revealed a high density of short fibers, most with lengths less than 1 μm (Appendix Figure 6a,b); for comparison, C_{16}-$(PEP_{Au}^{M\text{-}ox})_2$ typically assembles into much longer fibers (>5 μm) under the same conditions (Appendix Figure 5). Circular dichroism (CD) and Fourier transform infrared (FTIR) spectroscopy studies were conducted to investigate the molecular structure of these fibers. The CD spectrum of the modulator fibers exhibited a slight positive peak at ~198 nm and a negative peak at ~215 nm (Appendix Figure 6c) and the amide I stretch in the FTIR spectrum appeared at 1634 cm^{-1} (Appendix Figure 6d), which are consistent with β-sheet secondary structure.[59–62] In addition, a peak at ~2942 cm^{-1} in the FTIR spectrum corresponding to C-H stretches indicates the ordered packing of the aliphatic tails.[63] When C_{16}-$(AYSSGA)_2$ was incubated in Au NP helix synthesis and assembly conditions,[28] only discrete, nonassembled, Au NPs were observed (Appendix Figure 6e,f). These data confirm that modulator C_{16}-$(AYSSGA)_2$ assembles into fibers which do not direct the assembly of Au NPs.

Notably, the high density of short fibers suggests rapid fiber nucleation and growth, indicating that the modulator has a high propensity to assemble into fibers under the conditions studied.

We proceeded to explore how the addition of modulator to single helix syntheses affects length distribution. The mole ratio of C_{16}-$(PEP_{Au}{}^{M\text{-}ox})_2$ to modulator, X:Y, was varied between 10:1 and 10:25, where X and Y indicate nanomoles of C_{16}-$(PEP_{Au}{}^{M\text{-}ox})_2$ and C_{16}-$(AYSSGA)_2$, respectively, in the NP assembly reaction. The effect of modulator on single helix length is summarized in Table 1 and Figure 3. When only 1 nmol of modulator is added to a typical synthesis (10:1), the average helix length and distribution are similar to the control study (Figure 3a-c and Appendix Figures 7 and 8). However, increased amounts of modulator result in shorter helices and narrower helix length distribution. At ratios of 10:5 or higher, over 90% of the helices are shorter than 1000 nm. In general, the helix length distribution narrows as we increase the amount of modulator. For 10:5 (Figure 3e-g and Appendix Figures 9 and 10), only ~5.0% of the helices are longer than 1000 nm, the median length is ~385 nm, and the average length is ~442 nm, a distinctly different distribution compared to C_{16}-$(PEP_{Au}{}^{M\text{-}ox})_2$ alone. When we increase the amount of modulator to 10 nmol (10:10), only 1.3% of the helices are longer than 1000 nm, and the median and average lengths decrease to ~254 nm and ~296 nm, respectively (Figure 3i-k and Appendix Figures 11 and 12). At 10:15, when more modulator than C_{16}-$(PEP_{Au}{}^{M\text{-}ox})_2$ is present in solution, all measured helices are shorter than 1000 nm, with a median length of ~231 nm and an average length of ~261 nm (Figure 3m-o and Appendix Figure 13). When we increase modulator ratio even further, 10:25 (Appendix Figure 14 and 15), all counted helices are less than 1000 nm with 98.1%

Table 1. Helix length data of single helices prepared using C_{16}-$(PEP_{Au}^{M\text{-}ox})_2$ and mixtures of C_{16}-$(PEP_{Au}^{M\text{-}ox})_2$ and C_{16}-$(AYSSGA)_2$ (modulator)

mole ratio (nmol: nmol)		helix length			
C_{16}-$(PEP_{Au}^{M\text{-}ox})_2$	modulator	>1000 nm	< 500 nm	median (nm)	average (nm)
10	0[a]	~39.6%	~42.3%	~634	~1740
10	1[b]	~49.5%	~27.3%	~963	~1306
10	5[c]	~5.0%	~80.8%	~385	~442
10	10[d]	~1.3%	~92.0%	~254	~296
10	15[e]	~0%	~95.1%	~231	~291
10	25[f]	~0%	~98.1%	~174	~199
0	10	N/A	N/A	N/A	N/A

[a]measurement based on 260 structures; [b]measurement based on 143 structures; [c]measurement based on 199 structures; [d]measurement based on 377 structures; [e]measurement based on 304 structures; [f]measurement based on 214 structures.

shorter than 500 nm (Appendix Figure 16). The median and average lengths are ~174 and ~199 nm, respectively. Notably, short helices produced at ratios 10:5, 10:10, and 10:15 exhibit strong plasmonic chiroptical activity (Figure 3d,h,l,p and Appendix Figure 17 and 18), confirming that helix length, provided it completes at least one turn of the helix, should not impact the plasmonic coupling and the intensity of the plasmonic chiroptical response.[38] Helices formed from 10:25 did not show an observable plasmonic chiroptical response (Appendix Figure 19), perhaps due to the structural irregularity of the product (Appendix Figure 14 and 15). Further structural analysis of the helices indicates that increasing the amount of the modulator results in similar helical pitch length and, in general, similar NP dimensions (Appendix Table 1). We do note that the shortest helices produced from the 10:25 syntheses were less well-defined, and the NPs were more

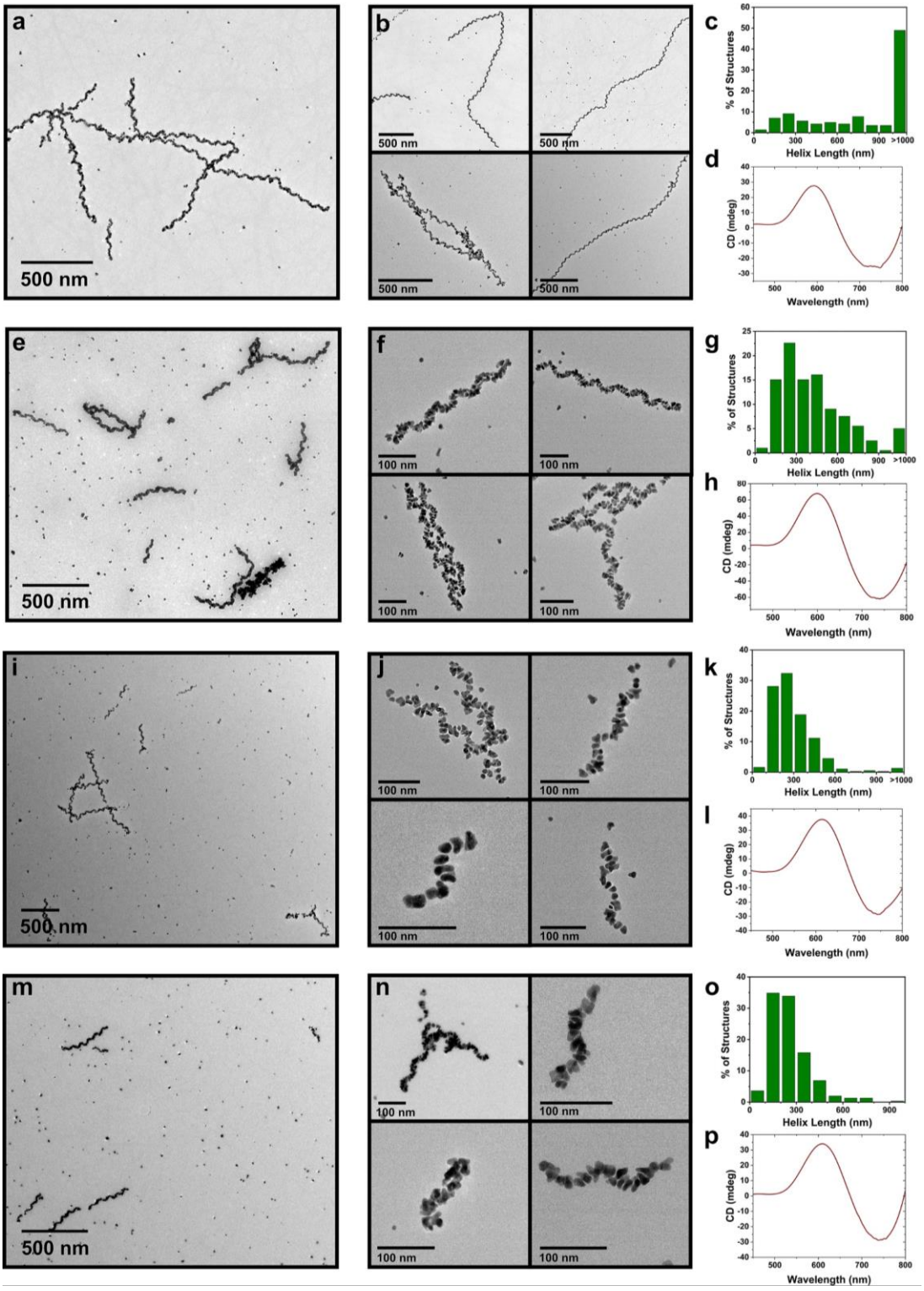

Figure 3.TEM images of Au NP single helices synthesized from C_{16}-$(PEP_{Au}^{M\text{-}ox})_2$: C_{16}- $(AYSSGA)_2$ at mole ratio of (a,b) 10:1 (e,f) 10:5 (i,j) 10:10 (m,n) 10:15. Helix length distribution of (c) 10:1 (g) 10:5 (k) 10:10 (o) 10:15; CD spectra of single helices (d) 10:1 (h) 10:5 (l) 10:10 (p) 10:15.

irregularly shaped; while we cannot definitively explain this phenomenon at this stage, we do comment on it further when we discuss the proposed mechanism of modulator-mediated length control (*vide infra*).

We also analyzed how modulator affects fiber length. A typical Au NP assembly experiment yields both Au NP single helices as well as undecorated peptide fibers. To visualize these fibers, we negatively stained the TEM grids for samples 10:1, 10:5, 10:10, and 10:25, collected TEM images (Appendix Figures 8, 10, 12, and 15), and then measured the fiber lengths. We found that fiber length distribution for each sample mirrored helix length distribution: an increasing amount of modulator resulted in shorter fiber length distribution (Appendix Figure 20 and Table 2). Fiber lengths are generally longer than 3000 nm for 10:1 (Appendix Figure 7). For 10:5, the median length is ~1005 nm, the average length is ~1093 nm, and ~50% of the fibers are shorter than 1000 nm (Appendix Figure S20). 10:5 exhibits shorter fiber length distribution than 10:1. With increasing amounts of modulator, the fiber lengths decrease. At 10:10, the average and median lengths are ~653 and ~547 nm, respectively, and ~80% of the fibers are shorter than 1000

Table 2. Fiber length data for C_{16}-$(PEP_{Au}{}^{M\text{-}ox})_2$ and mixtures of C_{16}-$(PEP_{Au}{}^{M\text{-}ox})_2$ and C_{16}-$(AYSSGA)_2$ (Modulator) (Measurement Based on 150 Counts)

Mole ratio (nmol:nmol)		Fiber length		
C_{16}-$(PEP_{Au}{}^{M\text{-}ox})_2$	Modulator	>1000 nm	median (nm)	average (nm)
10	1	~ 100%	-	-
10	5	~50%	~1005	~1093
10	10	~19.5%	~547	~653
10	25	~1%	~311	~348

nm (Appendix Figure 20 and Table 2). Most of the counted fibers were shorter than 1000 nm for 10:25, with an average length of ~348 nm and a median of ~311 nm (Appendix Figure 20 and Table 2). Thus, the addition of modulator results in shorter fiber lengths and length distributions overall.

As a first step toward understanding the modulator's role in reducing helix and fiber lengths, we conducted spectroscopic studies to determine whether it affects the molecular structure of the fibers. Fiber samples were prepared by incubating C_{16}-$(PEP_{Au}{}^{M\text{-}ox})_2$ with the modulator overnight in aqueous 4-(2-hydroxyethyl)-1-piperazineethanesulfonicic acid (HEPES) buffer at the ratios listed in Table 1. CD studies indicate that all samples have positive peaks at wavelength <200 nm and negative peaks between ~211 and 215 nm, indicating β-sheet secondary structure (Appendix Figure 21).[59,60] The strength of the signal generally correlates with the total concentration of peptide conjugate in the different samples. In addition, the FTIR spectra display an amide I band at ~1630 cm^{-1} and a C-H stretch at ~2920 cm^{-1}, which are characteristic of β-sheet secondary structure[61,62] and ordered packing of the hydrophobic tails,[63] respectively (Appendix Figure 22). These spectral data are consistent with what we have previously reported for C_{16}-$(PEP_{Au}{}^{M\text{-}ox})_2$ fibers,[33] suggesting that modulator does not disrupt the fibers' molecular structure.

We considered two possible pathways by which the molecular modulator might affect fiber growth and length as well as the length of the single-helical Au NP superstructures: i) molecular "capping" of fibers (Pathway 1) and ii) initiation of fiber nucleation (Pathway 2). The "capping" mechanism assumes that the modulator would competitively add to the growing ends of C_{16}-$(PEP_{Au}{}^{M\text{-}ox})_2$-based fibers and halt their growth; furthermore, it assumes that either C_{16}-$(PEP_{Au}{}^{M\text{-}ox})_2$ nucleation and growth precedes the modulator nucleation and growth or that they have similar assembly kinetics. The second proposed mechanism considers the strong assembly propensity of

the modulator due to its hydrophobic to hydrophilic ratio, and its ability to promote rapid formation of nucleation seeds onto which C_{16}-$(PEP_{Au}{}^{M\text{-}ox})_2$ may associate and then grow into fibers. Thus, the modulator would accelerate C_{16}-$(PEP_{Au}{}^{M\text{-}ox})_2$ fiber growth, resulting in short fiber and helix length distribution.

To distinguish between these two proposed pathways, we conducted Thioflavin T (ThT) fluorescence assays to examine how modulator influences fiber growth kinetics,[64,65] reasoning that Pathway 2, in which the modulator is postulated to rapidly nucleate to yield "nucleation seeds" for fiber growth, would be supported by observation of rapid growth kinetics and large populations of shorter fibers. The ThT fluorescence profile for C_{16}-$(PEP_{Au}{}^{M\text{-}ox})_2$ assembly exhibits a sigmoidal curve consisting of a lag phase (0-60 min), an elongation phase (60-660 min), and an equilibrium

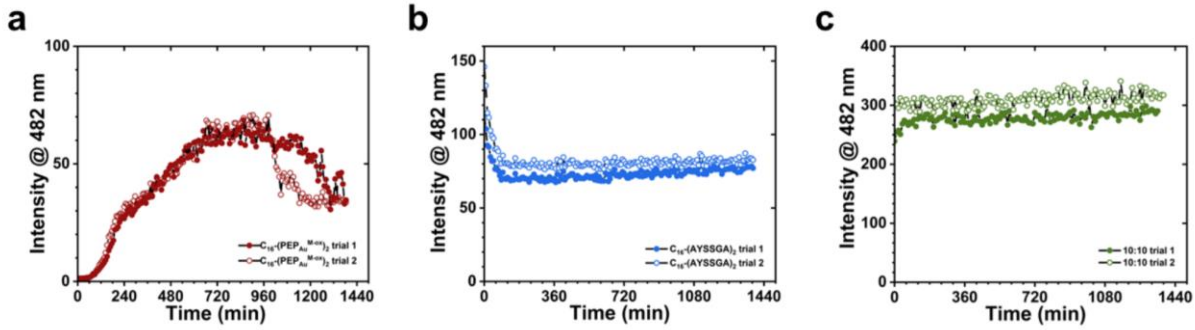

Figure 4. Thioflavin T (ThT) fluorescence monitoring of the assembly of (a) two replicates of C_{16}-$(PEP_{Au}{}^{M\text{-}ox})_2$, (b) two replicates of C_{16}-$(AYSSGS)_2$, and (c) two replicates of 10:10 C_{16}-$(PEP_{Au}{}^{M\text{-}ox})_2$: C_{16}-$(AYSSGS)_2$.

phase (660-1380 min) (Figure 4a), which suggests that C_{16}-$(PEP_{Au}{}^{M\text{-}ox})_2$ undergoes cooperative supramolecular polymerization.[66] In comparison, the modulator alone exhibits a dramatically different fluorescence profile, with an immediate equilibrium stage and without observable nucleation and elongation stages (Figure 4b). The apparent instantaneous assembly in aqueous buffer can be understood when considering that the modulator, C_{16}-$(AYSSGS)_2$, contains only the "assembly" components of C_{16}-$(PEP_{Au}{}^{M\text{-}ox})_2$ and has a high hydrophobic to hydrophilic ratio.

However, the modulator does exhibit supramolecular cooperative assembly consisting of i) nucleation stage (0-60 min) ii) elongation stage (60-90 min), and iii) equilibrium stage (90 min and beyond) when its assembly is monitored in a more hydrophobic solution environment, 1:1 acetonitrile/H_2O (Appendix Figure 23).

We collected TEM images at different timepoints along the fiber assembly profile to track fiber growth and the evolution of fiber length. For C_{16}-$(PEP_{Au}^{M\text{-}ox})_2$, at t = 0, which corresponds to the onset of the nucleation phase, we observed little fiber formation (Appendix Figure 24a). During the fiber growth phase, at t = 1, 2, and 3 h, we observed long fibers (>3 μm) and increasing fiber density on the TEM grids (Appendix Figure 24b-d). At 18h, during the equilibrium phase, we again observe a dense network of long fibers (Appendix Figure 24e). In the case of the modulator, TEM images collected at t = 0 show a high density of short fibers (Appendix Figure 25a), which would be expected if there were an initial burst of nucleation sites followed by fiber growth. Modulator fibers are significantly shorter than C_{16}-$(PEP_{Au}^{M\text{-}ox})_2$ fibers, with an average and median length of ~485 nm and ~400 nm, respectively at 1h and ~999 nm and ~910 nm at 3h (Appendix Table 2).

The ThT fluorescence profile of the 10:10 mixture of C_{16}-$(PEP_{Au}^{M\text{-}ox})_2$ and modulator indicates immediate nucleation following by elongation (0-1 h) and then equilibrium (1 hr and beyond) (Figure 4c). TEM fiber length monitoring of this sample reveals a high density of short fibers (median and average fiber length <600 nm) at t = 0 and 30 min (Figure S26a-b and Table S3). At t = 4 h, we observed a slight increase in fiber length, with average and median of ~926 nm and ~720 nm, respectively (Appendix Table 3 and Appendix Figure 26e). Overall, the 10:10 sample exhibits a significantly shorter fiber length distribution and a much more rapid assembly profile compared to C_{16}-$(PEP_{Au}^{M\text{-}ox})_2$ alone. To further examine the influence of the modulator, we

conducted the ThT fluorescence assay for a 10:20 sample (Appendix Figure 27). Its assembly profile is similar to that observed for 10:10 with immediate nucleation, followed by elongation (0-300 min), and lastly equilibrium (300-1380 min). 10:20 exhibits shorter fibers compared to 10:10 and pure C_{16}-$(PEP_{Au}{}^{M\text{-}ox})_2$, with median and average fiber lengths of <500 nm at t = 0 min, 1, 3, and 48 h (Appendix Figure 28 and Appendix Table 4).

From these mechanistic studies, we conclude that the modulator, a β-sheet assembly agent, nucleates rapidly, yielding numerous seeds to which free conjugates can add to form fibers. This results in a large population of short fibers (Pathway 2). When the modulator is added to C_{16}-$(PEP_{Au}{}^{M\text{-}ox})_2$, it promotes rapid nucleation and growth; the modulator nuclei can serve as seeds for growth of both C_{16}-$(PEP_{Au}{}^{M\text{-}ox})_2$ and modulator fibers, and potentially fibers containing a mixture of the modulator and C_{16}-$(PEP_{Au}{}^{M\text{-}ox})_2$. Since C_{16}-$(PEP_{Au}{}^{M\text{-}ox})_2$ contains the same assembly module as the modulator, it is reasonable to assume that monomers of C_{16}-$(PEP_{Au}{}^{M\text{-}ox})_2$ could add to the modulator nuclei. We postulate that syntheses containing a larger amount of modulator (*e.g.*, 10:25) yield fibers constructed from a significant amount of modulator. Since the modulator does not contain the particle-binding module which helps cap particle growth, the helices that form on these fibers are composed of more irregularly shaped particles (*vide supra*).

2.3 Conclusions

We established that a molecular modulator approach can be used to control amphiphilic peptide conjugate fiber growth profiles and can be leveraged to control the length of fibers and helical Au NP assemblies. The introduction of modulator C_{16}-$(AYSSGA)_2$ to the C_{16}-$(PEP_{Au}{}^{M\text{-}ox})_2$ Au NP assembly system significantly affects the length of single-helical superstructures: as the

amount of the modulator increases with respect to a fixed concentration of C_{16}-$(PEP_{Au}{}^{M\text{-}ox})_2$, peptide conjugate fiber length and Au NP superstructure length decrease. ThT fluorescence kinetic studies and fibril length evolution imaging provided mechanistic insights that suggest that modulator accelerates the nucleation kinetics of the entire assembly system, leading to overall shorter fiber lengths. We used this molecular modulator approach to achieve single-helix samples with average and median helix lengths between ~200-500 nm and ~200-400 nm, respectively. Significantly, these samples maintained the intense plasmonic chiroptical response which has previously been observed for samples generated from unmodulated syntheses.

3.0 Materials and Methods

3.1 Materials

All chemicals were purchased from commercial sources and used without purification unless otherwise noted. Fmoc-protected amino acids (Fmoc = fluorenylmethyloxycarbonyl), Fmoc-protected Phe and Ala NovaSyn®TGA resins, and O-(1H-6-Chloro-benzotriazole-1-yl)-1,1,3,3-tetramethyluronium hexafluorophosphate (HCTU) were purchased from Novabiochem®; Dialysis mini tubes (D-tube™) were purchased from EMD Millipore; N,N-dimethylformamide (DMF), methylene chloride (DCM), and 1.0 M 4-(2-hydroxyethyl)-1-piperazineethanesulfonic acid (HEPES) buffer (pH = 7.3 ± 0.1) were purchased from Fisher Chemical; diethyl ether (Et_2O, 99.5%, extra dry, stabilized, AcroSeal®), trifluoroacetic acid (TFA, 99% extra pure), and Thioflavin T (ThT) dye were purchased from Acros Organics; 5-azidovaleric acid was purchased from TCI Chemical; formic acid (88%, Baker analyzed®) was purchased from JT Baker. Carbon support film (5-6 nm thick, 400 mesh) copper grids were purchased from Electron Microscopy Sciences. All other chemicals were purchased from Sigma-Aldrich. Nanopure water (18.1 mΩ, Barnstead Diamond™ purification system) was used for all aqueous studies.

3.2 Reverse-Phase High-Pressure Liquid Chromatography Purification

All synthesized peptides and peptide conjugates were purified under ambient temperature using an Agilent 1200 liquid chromatographic system equipped with diode array and multiple-wavelength detectors and using a Zorbax-300SB C_{18} column. A linear gradient of a binary solvent system (A: 0.1% formic acid in Nanopure water; B: 0.05% formic acid in acetonitrile) ramping from 95% buffer A and 5% buffer B to 5% buffer A and 95% buffer B over a period of 30 mins was used to purify the peptides and peptide conjugates.

3.3 UV-Vis Spectroscopy

All synthesized peptides and peptide conjugates were quantified based on the absorbance of Tyrosine (1280 M^{-1} cm^{-1}) at 280 nm. UV-Vis absorption spectra were collected using an Agilent 8453 UV-Vis spectrometer equipped with deuterium and tungsten lamps and using a quartz cuvette with 10 mm path length.

3.4 Liquid Chromatography-Mass Spectroscopy

LC-MS spectra were collected on a Shimadzu LCMS-2020 instrument using a direct injection method with an electron spray ionization (ESI) probe in positive and negative scan mode over a total run of 6 mins.

3.5 Fmoc Solid-Phase Peptide Synthesis

Peptides were synthesized by manual solid-phase peptide synthesis (SPSS) using a CEM MARS microwave (Mattews, NC, USA) and NovaSyn® TGA Fmoc resin. The synthesis protocol consists of i) resin preparation and deprotection, ii) sequential amino acid coupling followed by Fmoc-deprotection, iii) capping of 5-azido pentanoic acid to the N-terminus and iv) peptide cleavage from resin. To activate the amino acids, HCTU (5 equiv. to resin) and N,N-Diisopropylethylamine (DIEA) (7 equiv. to resin) in 1-methyl-2-pyrrolidinone (NMP) were added to Fmoc-protected amino acids (5 equiv. to resin) and allowed to sit for 5-7 min. The coupling reaction occurred under 1 min ramp from room temperature to 75°C followed by a 5 min hold. The deprotection solutions consisted of 20% v/v 4-methylpiperidine in DMF, and the reaction proceeded under a 1 min ramp to 75°C followed by a 2 min hold. To cap the N-terminus, 5-azidovaleric acid (5 equiv. to resin) was activated and coupled following the typical procedure (no final deprotection). The resin was then washed with DMF (3X), DCM (3X), methanol (3X), and then dried under vacuum for 30 min. To cleave the peptide, the resin was soaked in a peptide cleavage cocktail (90% TFA, 5% triisopropylsilane (TIS), and 5% Nanopure H_2O) for 4 h. Cold

Et_2O was added to precipitate the peptide. After centrifugation, the supernatant was decanted and 1:1 acetonitrile(ACN):H_2O was added to dissolve the pellet. The peptide solution was lyophilized using a Labconco Freeze-Dryer system (Kansas City, MO, USA) and the solid peptide was stored at -20 °C.

3.6 Peptide Conjugate Synthesis

Detailed protocols can be found in previous reports.[28,31] Briefly, oxidized N_3-$PEP_{Au}^{M\text{-}ox}$ was prepared by adding 8 µl of 50% hydrogen peroxide (H_2O_2) solution to ~5mg of peptide dissolved in 1 mL of 1:1 ACN:H_2O. C_{16}-dialkyne was attached to each azido-terminated peptide sequence via copper-catalyzed cycloaddition to synthesize C_{16}-$(PEP_{Au}^{M\text{-}ox})_2$ and modulator, C_{16}-$(AYSSGA)_2$.

3.7 Fiber Assembly

250 µl of 0.1 M HEPES buffer was added to lyophilized peptide conjugates. The solution was sonicated for 5 min. 2.5 µl of 0.1 M calcium chloride ($CaCl_2$) was then added to promote assembly.

3.8 Au NP Helix Assembly

250 µl of 0.1 M HEPES buffer was added to lyophilized peptide conjugates. For short helices preparation, the peptide conjugates consisted of mixture of C_{16}-$(PEP_{Au}{}^{M\text{-}ox})_2$ and modulator (C_{16}-$(AYSSGA)_2$) at appropriate nanomole ratios. The solution was sonicated for 5 min, 2.5 µl of 0.1 M $CaCl_2$ was added, and the solution was left undisturbed for 25 mins. 1 µl of a gold precursor solution (1:1 1.0 M triethylammonium acetate buffer (TEAA):0.1 M aqueous gold (III) chloride trihydrate ($HAuCl_4$)) was added. A black precipitate forms after ~2 sec, at which time the solution was immediately vortexed for ~30 seconds. The solution was allowed to sit undisturbed for 16 hours before further characterization.

3.9 CD Spectroscopy

Circular dichroism (CD) studies were performed on an Olis DSM 17 CD spectrometer with a quartz cuvette (1 mm path length) at 25 ºC with 8 nm/min scan rate and 2 nm bandwidth. For secondary structure studies, solid peptide conjugates were dissolved in 0.01 M HEPES and spectra were collected from 190 to 250 nm. For plasmonic studies, spectra were collected from 450 to 800 nm.

3.10 Attenuated Total Reflectance Fourier Transform Infrared Spectroscopy

ATR-FTIR spectra were collected on a PerkinElmer Spectrum 100 spectrometer (Waltham, MA, USA) equipped with a universal attenuated total reflectance sampling accessory. Spectra were collected between 450-4000 cm^{-1} and processed using PerkinElmer Spectrum Express software. Peptide conjugates were dissolved in 0.1 M HEPES for one day, then, the fibers were dialyzed in Nanopure H_2O using a dialyzer mini tube (Millipore, D-Tube^{TM}, MWCO 12-14 kDa, catalog No. 71505-3). The samples were concentrated by air evaporation. 1 µl of the concentrated samples was drop-cast onto ATR crystal surface and allowed to air dry. The collected spectra were background-corrected in air.

3.11 Transmission Electron Microscopy

C_{16}-$(PEP_{Au}^{M\text{-}ox})_2$ and "10:10" negatively-stained images were collected on a FEI Morgagni 268 instrument operated at 80 KV and equipped with an AMT side mount CCD camera system. The remaining TEM images were collected on a Hitachi H-9500 microscope (Chiyoda, Tokyo, Japan) equipped with Gatan CCD camera analyzed by Digital Micrograph software operating at 300 KV. Previously reported sample preparation protocols were used.[28,33] All TEM image measurements were analyzed using ImageJ (NIH, USA) software.[67,68]

3.12 ThT Assays

Thioflavin T (ThT) fluorescence assays were conducted in 96-well flat bottom black plate (Greiner Bio-One, catalog No.655209) at 26 ºC in Tecan Infinite M1000 Pro fluorescence plate reader. Lyophilized peptide conjugates were dissolved in 250 µl of 5 µM ThT in 0.1 M HEPES buffer and 2.5 µl of 0.1 M $CaCl_2$ was added. After brief vortexing, the sample solution was transferred to each well. The ThT fluorescence kinetic profile was recorded with either 5 min or 8 min reading intervals and 5 s shaking (3 mm in linear amplitude, 372-414 rpm in linear frequency) before each read (440 nm excitation, 482 nm emission). At least two replicates were collected for each assay. All fluorescence spectra signals were background corrected.

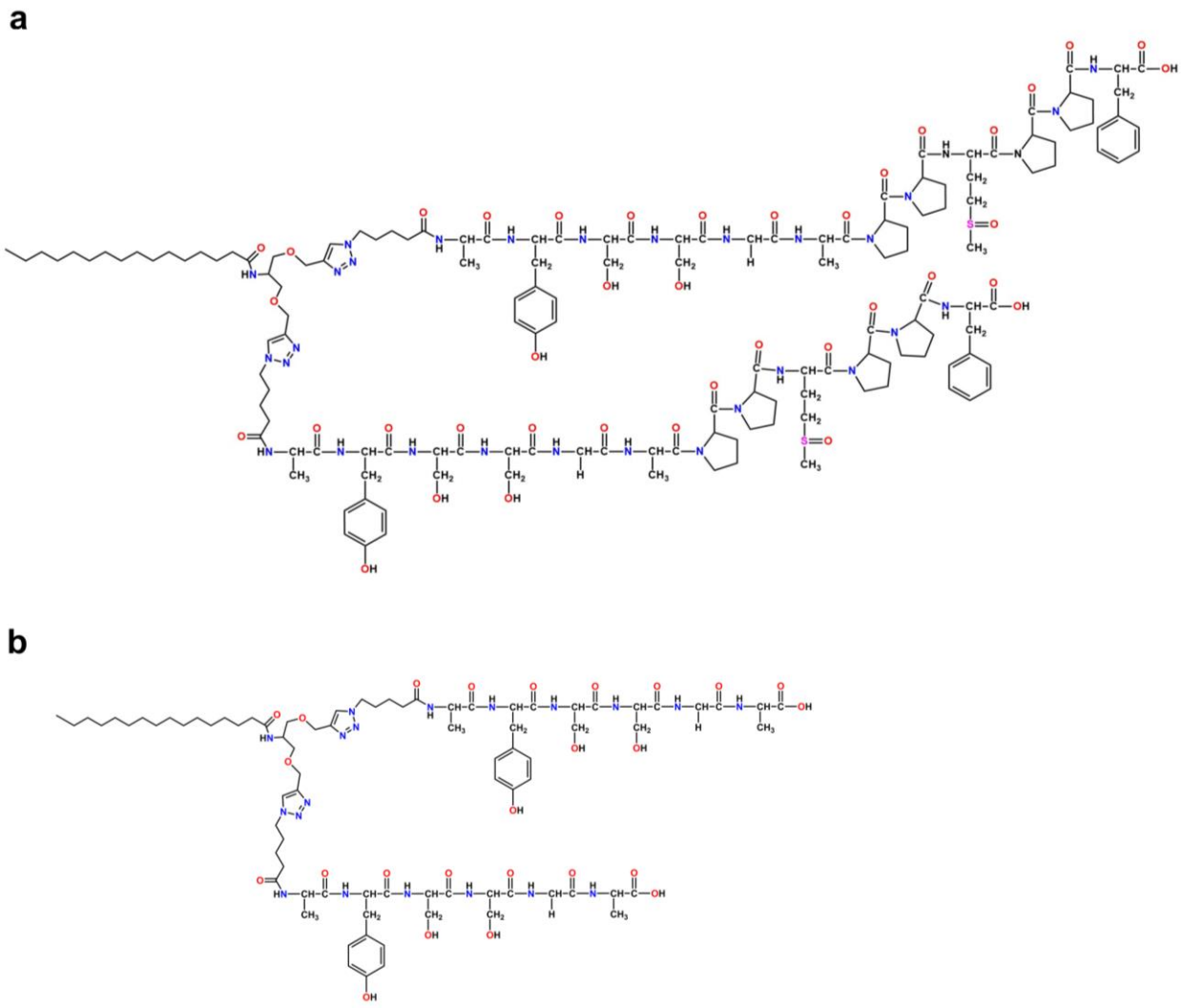

Appendix Figure 1. Chemical structures of (a) C_{16}-($PEP_{Au}^{M\text{-}ox}$)$_2$ and (b) C_{16}-(AYSSGA)$_2$.

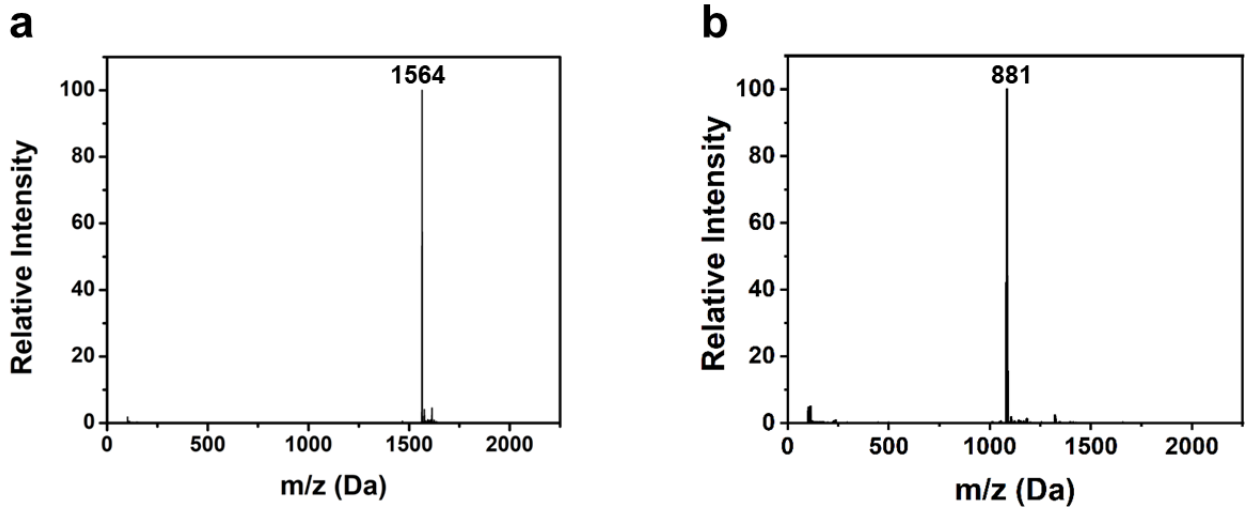

Appendix Figure 2. LC-MS spectra of (a) C_{16}-($PEP_{Au}^{M\text{-}ox}$)$_2$, m/z = 1564 Da ($M\text{-}2H^+$)/2 and (b) C_{16}-(AYSSGA)$_2$, m/z= 881 Da ($M\text{-}2H^+$)/2).

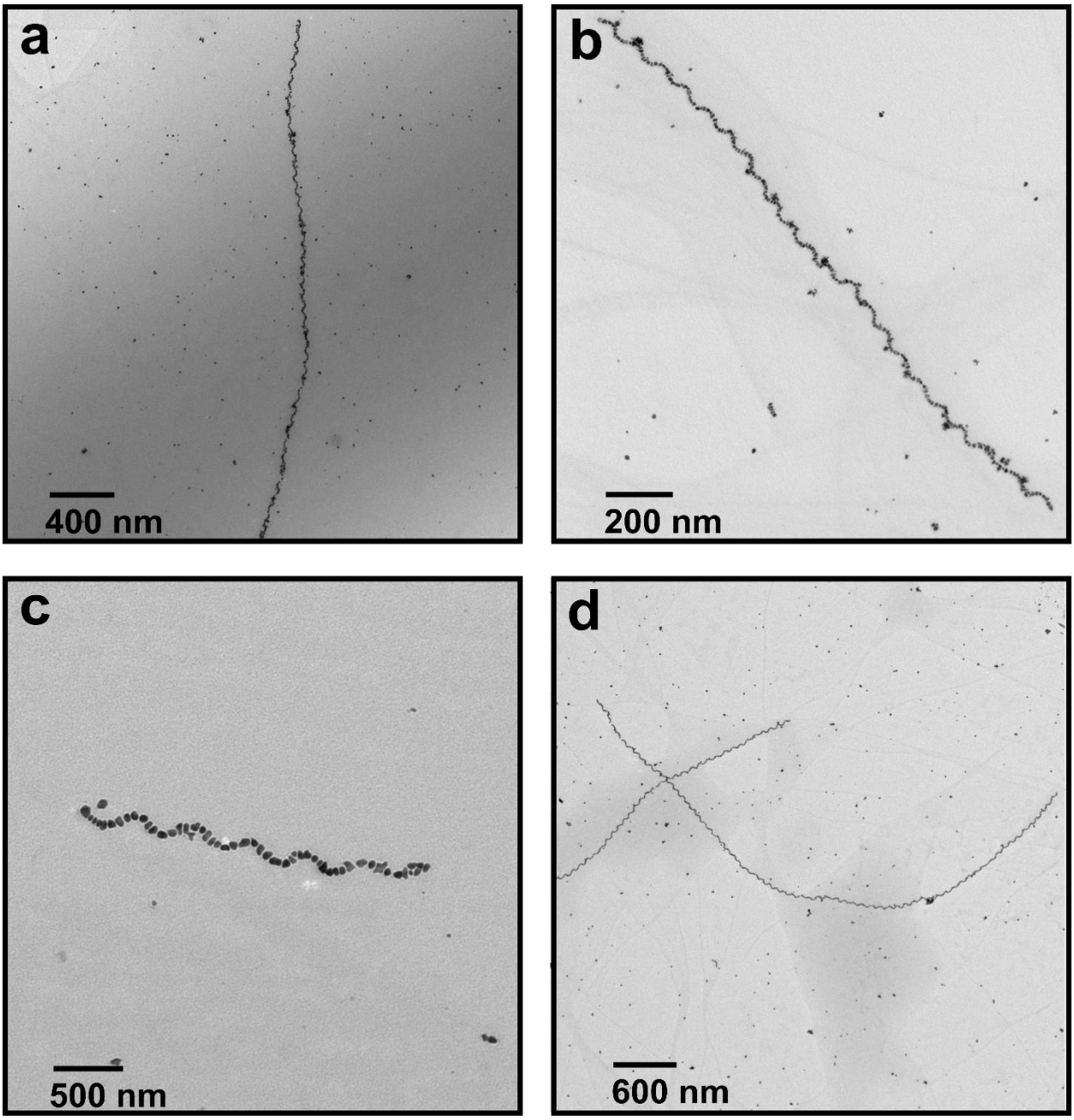

Appendix Figure 3. Representative TEM images of single helices fabricated using C_{16}-$(PEP_{Au}^{M\text{-}ox})_2$. These images, and others, were used for determining the helix length distribution.

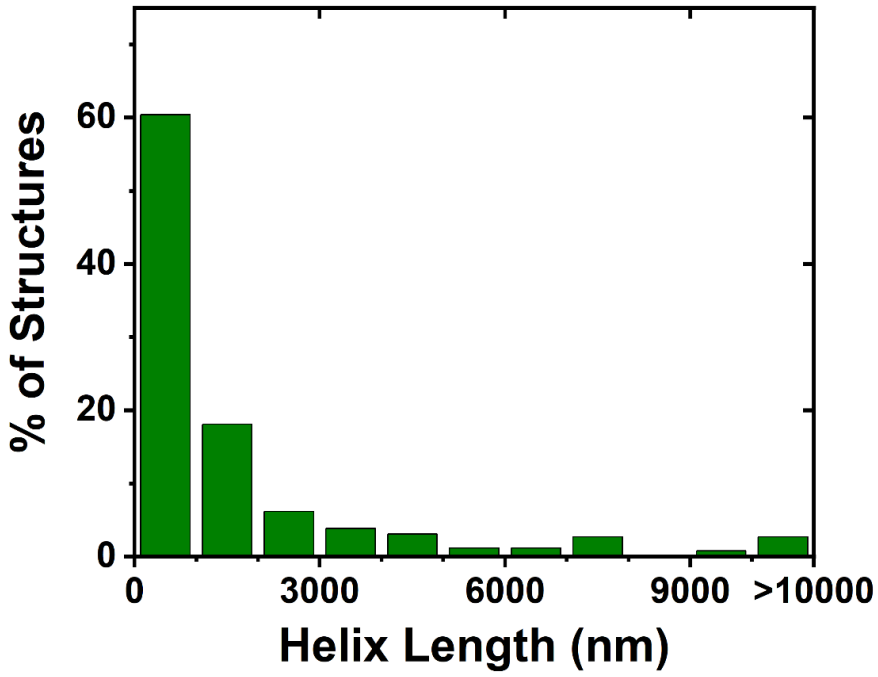

Appendix Figure 4. Helix length distribution for single helices prepared using C_{16}-$(PEP_{Au}^{M\text{-}ox})_2$. Helix lengths ranged from ~80-25000 nm with an average of ~1740 nm and median of 693 nm. 39.6% superstructures are longer than 1000 nm. Measurement is based on 260 counts.

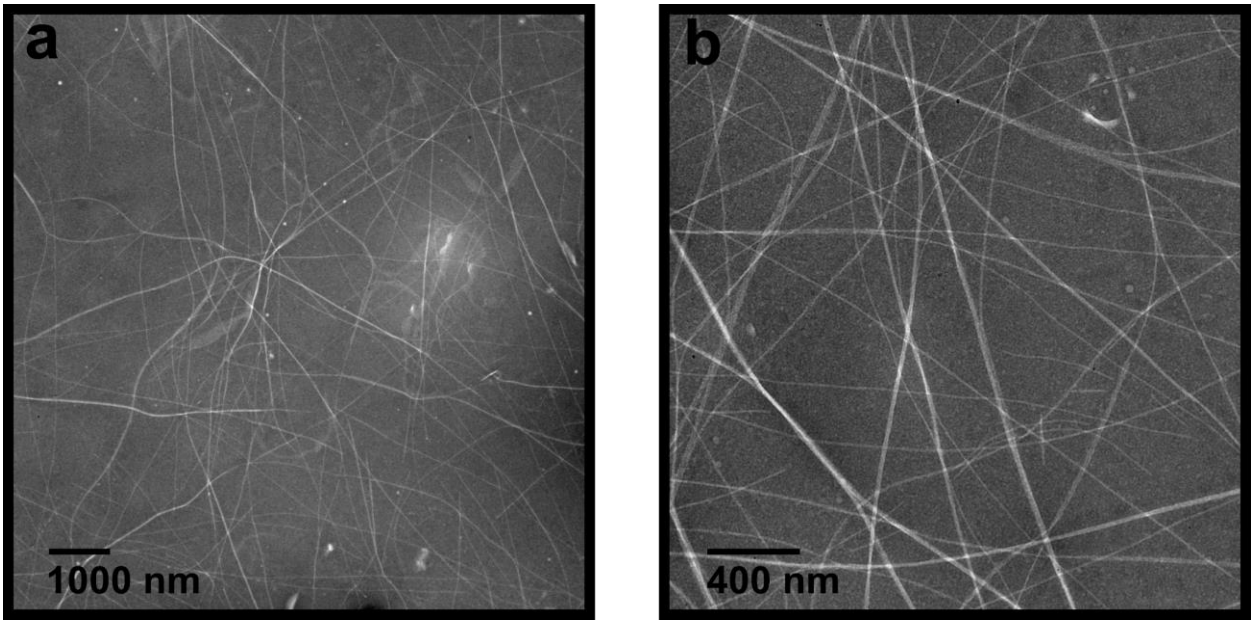

Appendix Figure 5. Representative negatively-stained TEM images of C_{16}-$(PEP_{Au}^{M\text{-}ox})_2$-based fibers. These images, and others, were used for determining the fiber length distribution

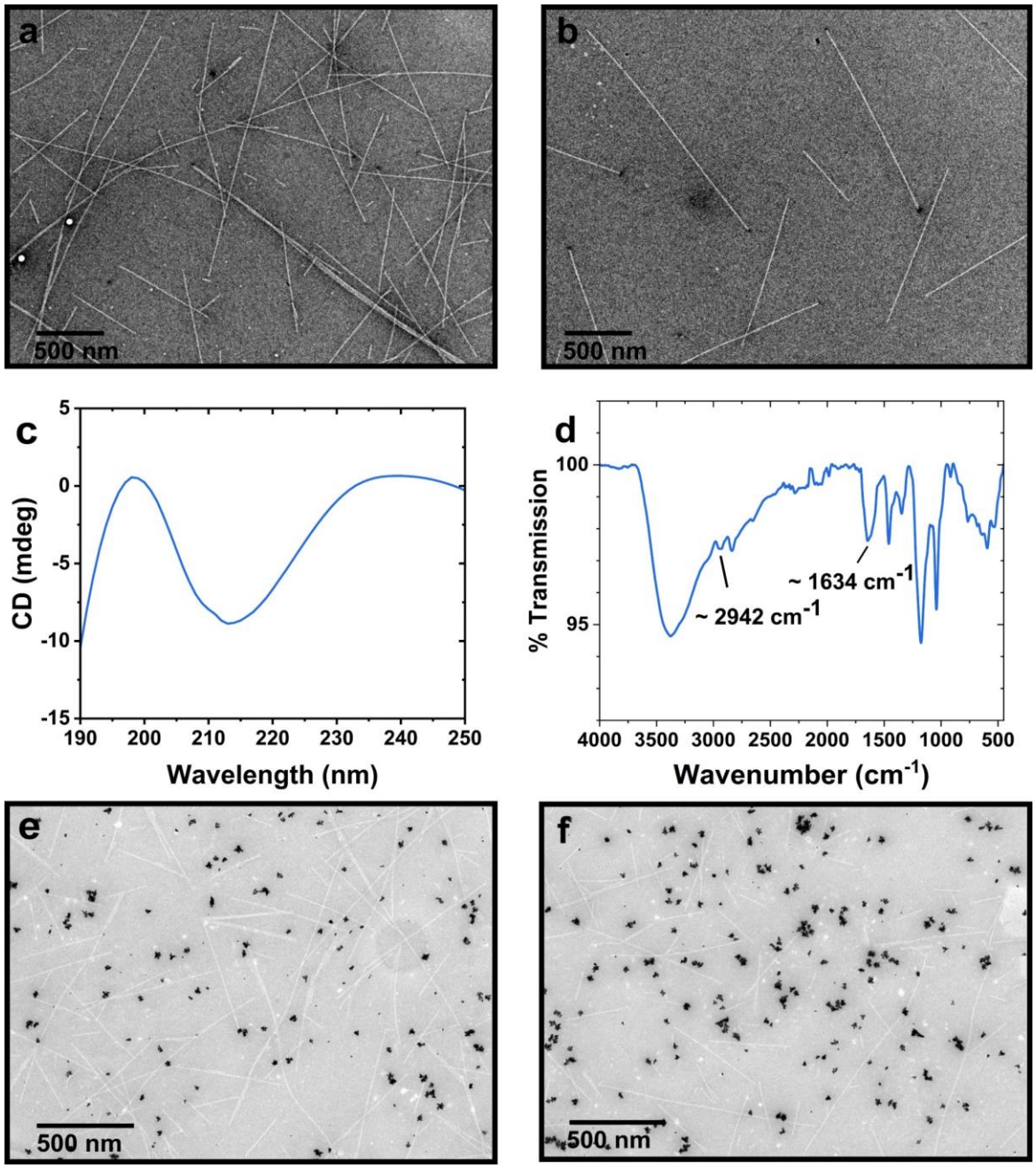

Appendix Figure 6 C_{16}-$(AYSSGA)_2$ fiber formation studies and Au NP-binding studies. (a,b) Negatively-stained TEM images of C_{16}-$(AYSSGA)_2$-based fibers. (c) CD spectrum and (d) FT-IR spectrum of fibers. (e,f) Negatively-stained TEM images of samples in which C_{16}-$(AYSSGA)_2$ was subjected to typical single helix synthesis conditions. No NP assemblies are observed, and the Au NP do not associate with the C_{16}-$(AYSSGA)_2$-based fibers.

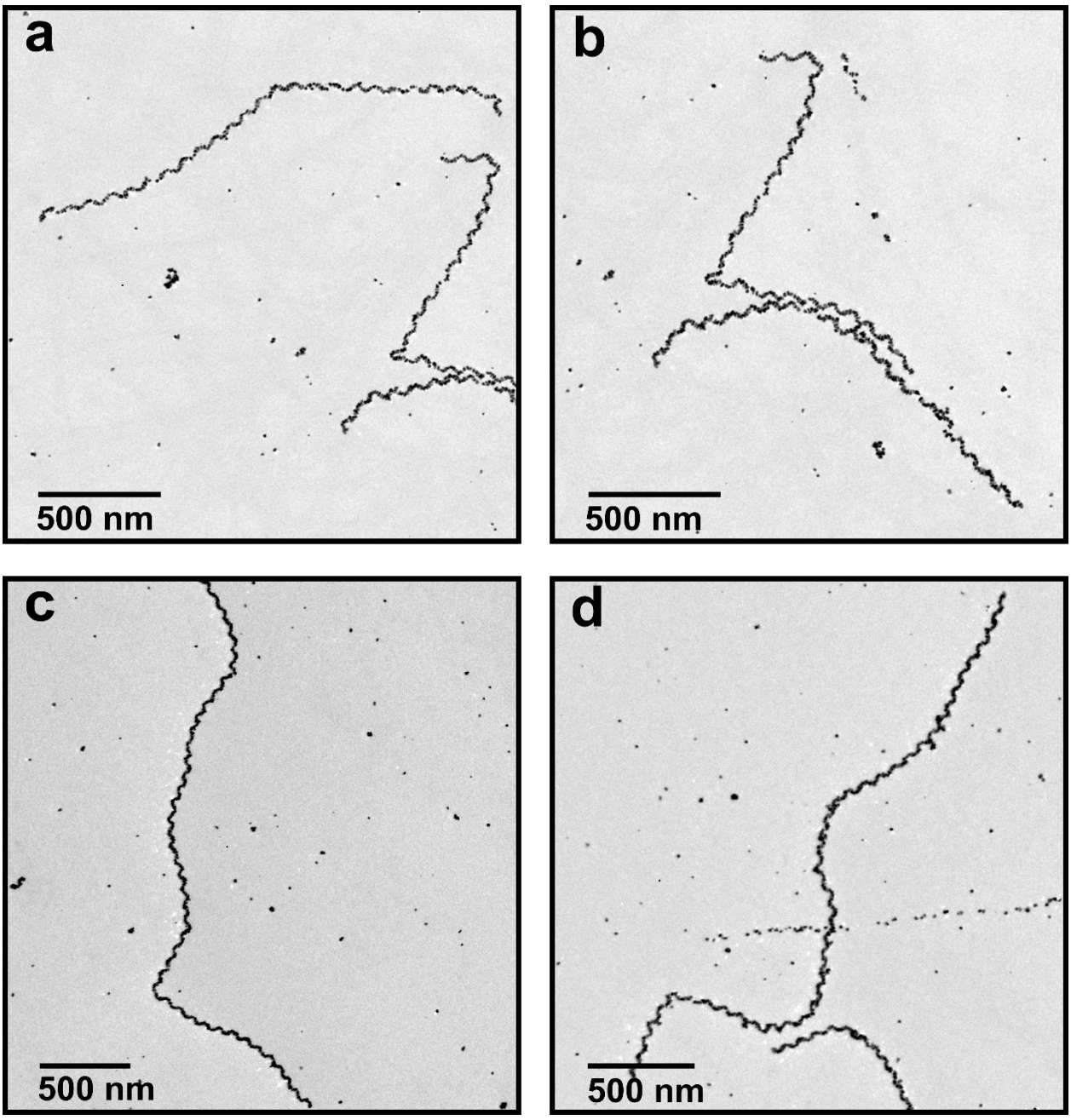

Appendix Figure 7 Additional TEM images of Au NP single helices formed using 10:1 C_{16}-$(PEP_{Au}^{M\text{-}ox})_2$: C_{16}-$(AYSSGA)_2$. These images, and others, were used for determining the helix length distribution.

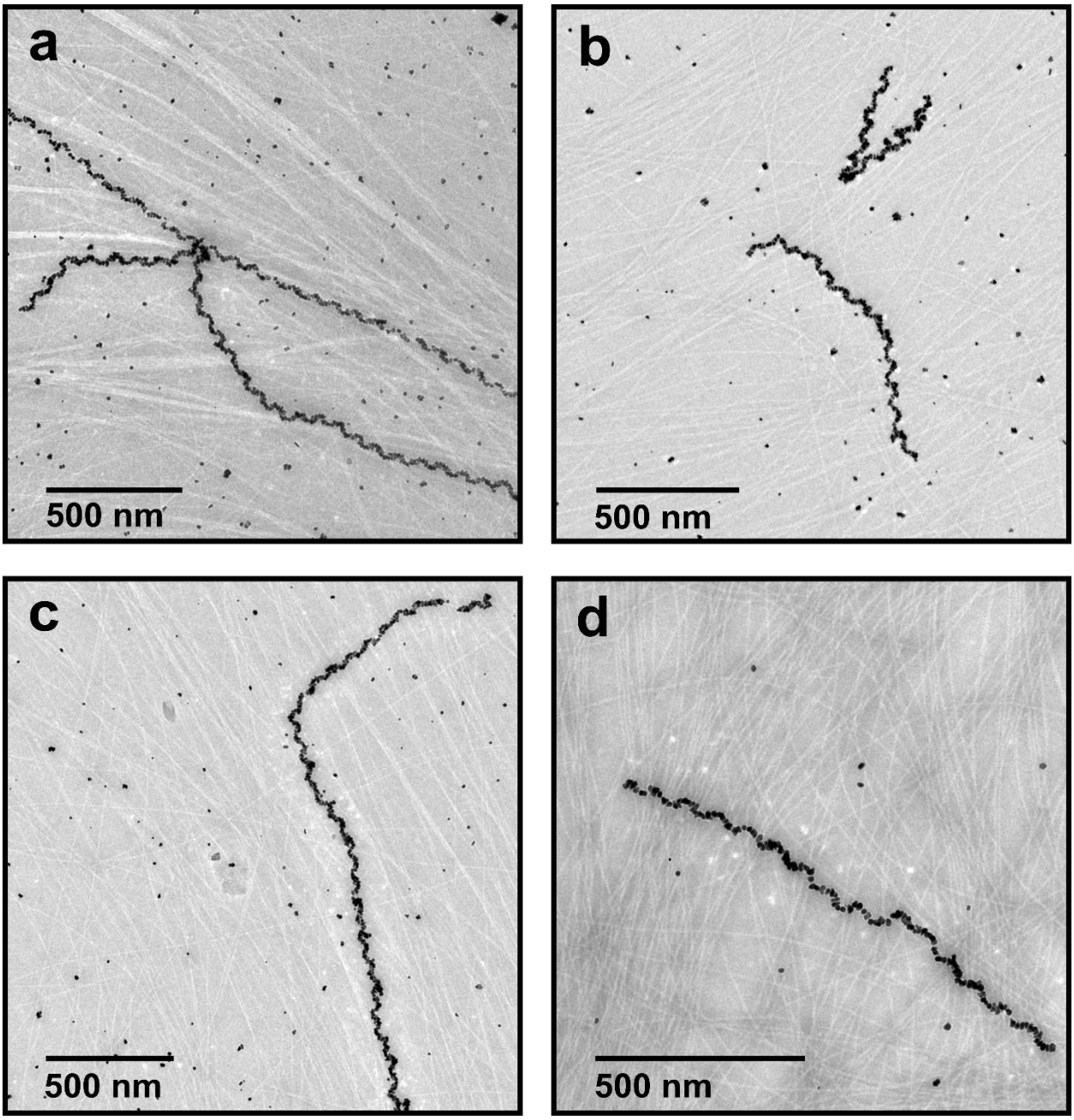

Appendix Figure 8 Negatively-stained TEM images of Au NP single helices formed using 10:1 C_{16}-$(PEP_{Au}^{M\text{-}ox})_2$: C_{16}-$(AYSSGA)_2$. These images, and others, were used for determining the fiber length distribution.

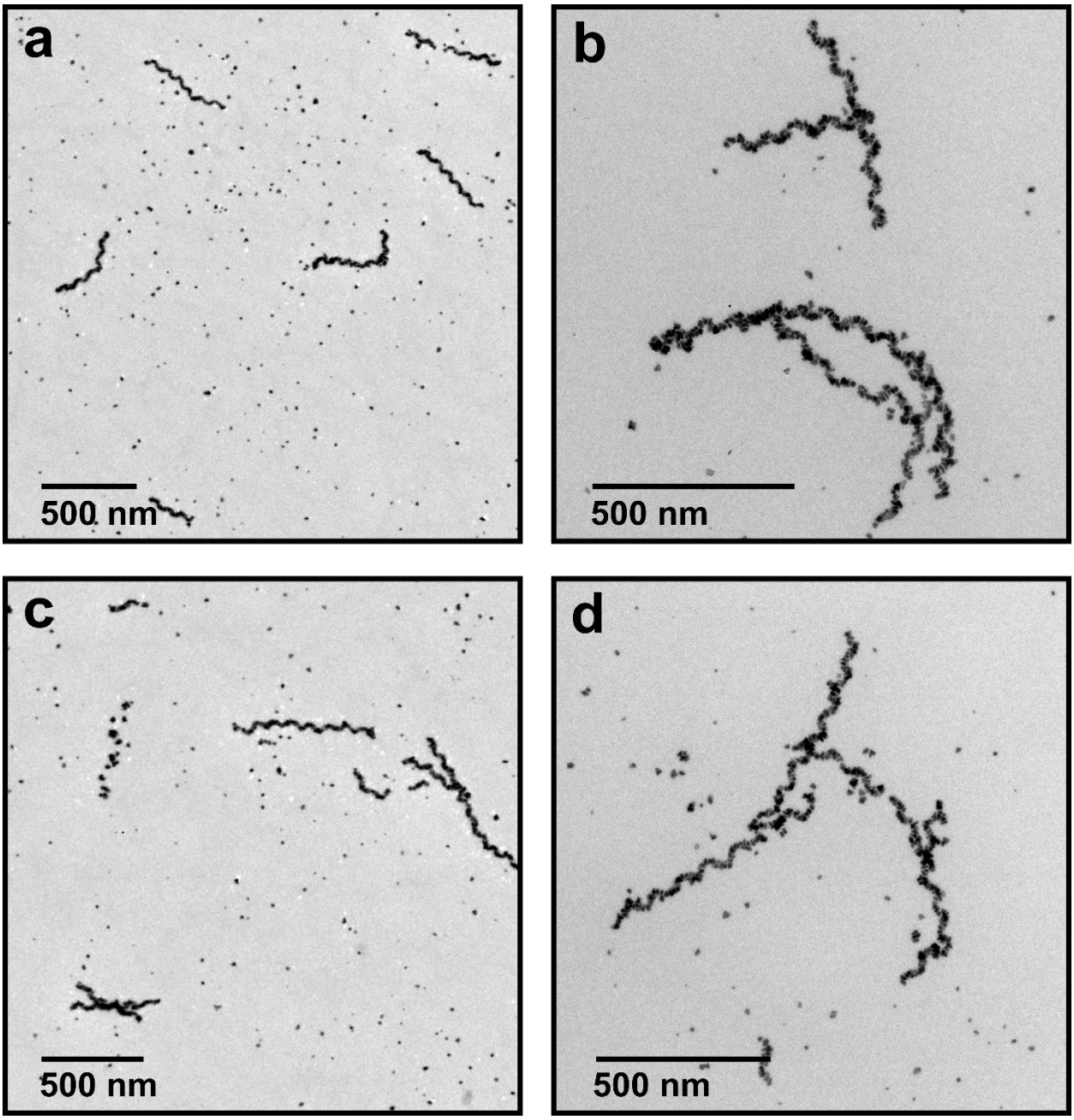

Appendix Figure 9 Additional TEM images of Au NP single helices formed using 10:5 C_{16}-$(PEP_{Au}^{M\text{-}ox})_2$: C_{16}-$(AYSSGA)_2$. These images, and others, were used for determining the helix length distribution.

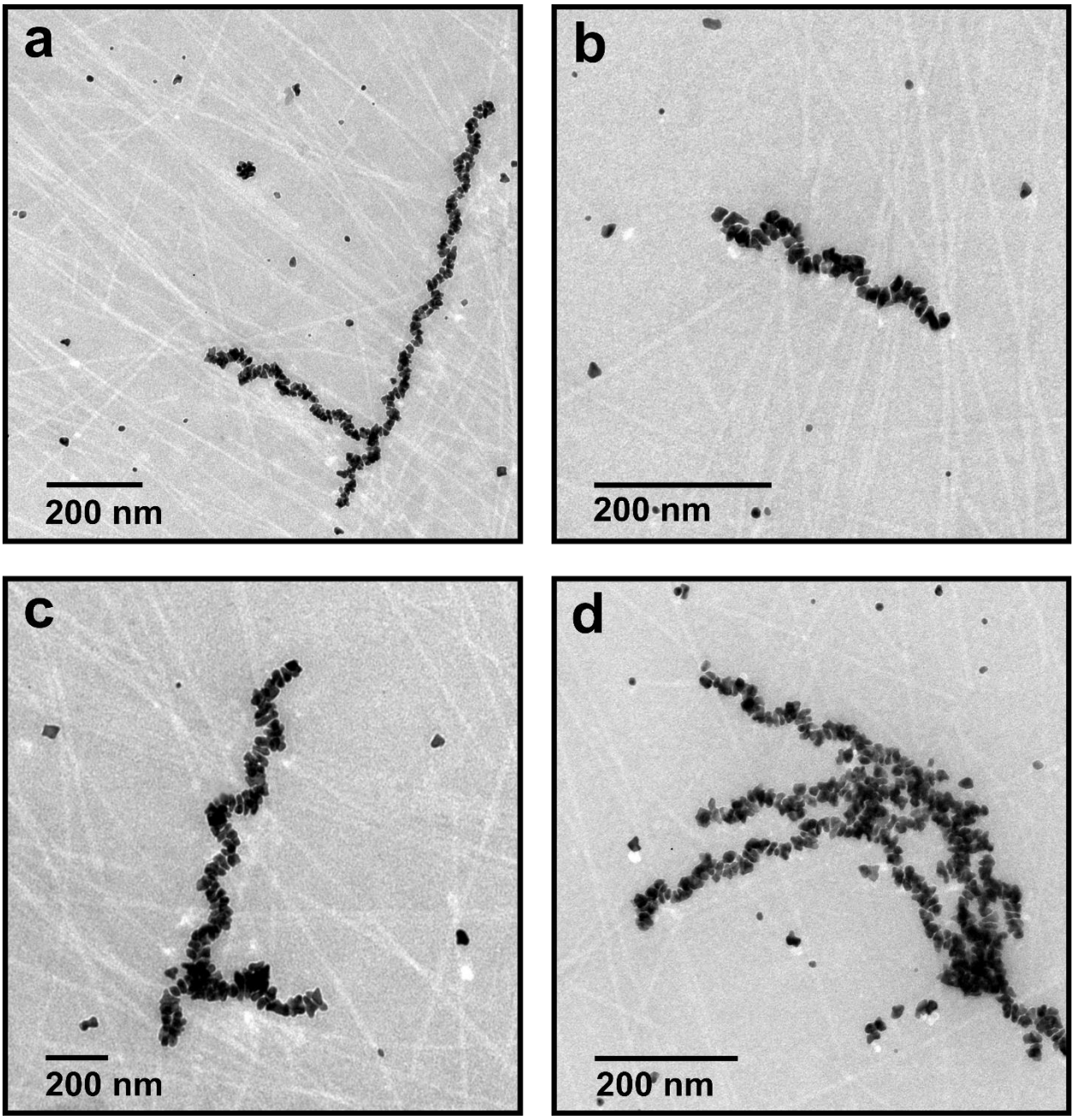

Appendix Figure 10 Negatively-stained TEM images of Au NP single helices formed using 10:5 C_{16}-(PEP_{Au}^{M-ox})2 : C_{16}-$(AYSSGA)_2$. These images, and others, were used for determining the fiber length distribution.

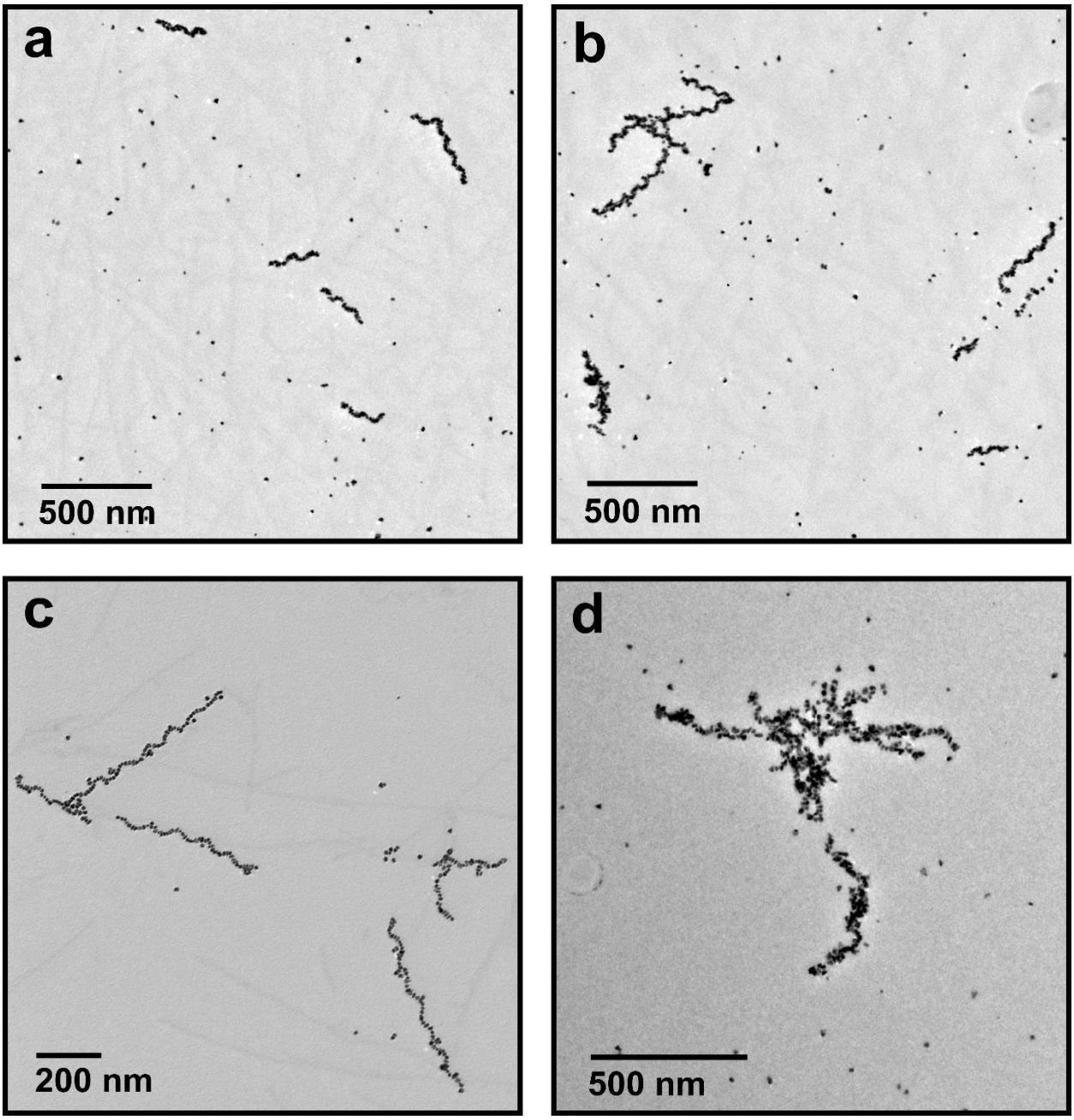

Appendix Figure 11 Additional TEM images of Au NP single helices formed using 10:10 C_{16}-$(PEP_{Au}^{M\text{-}ox})_2$: C_{16}-$(AYSSGA)_2$. These images, and others, were used for determining the helix length distribution.

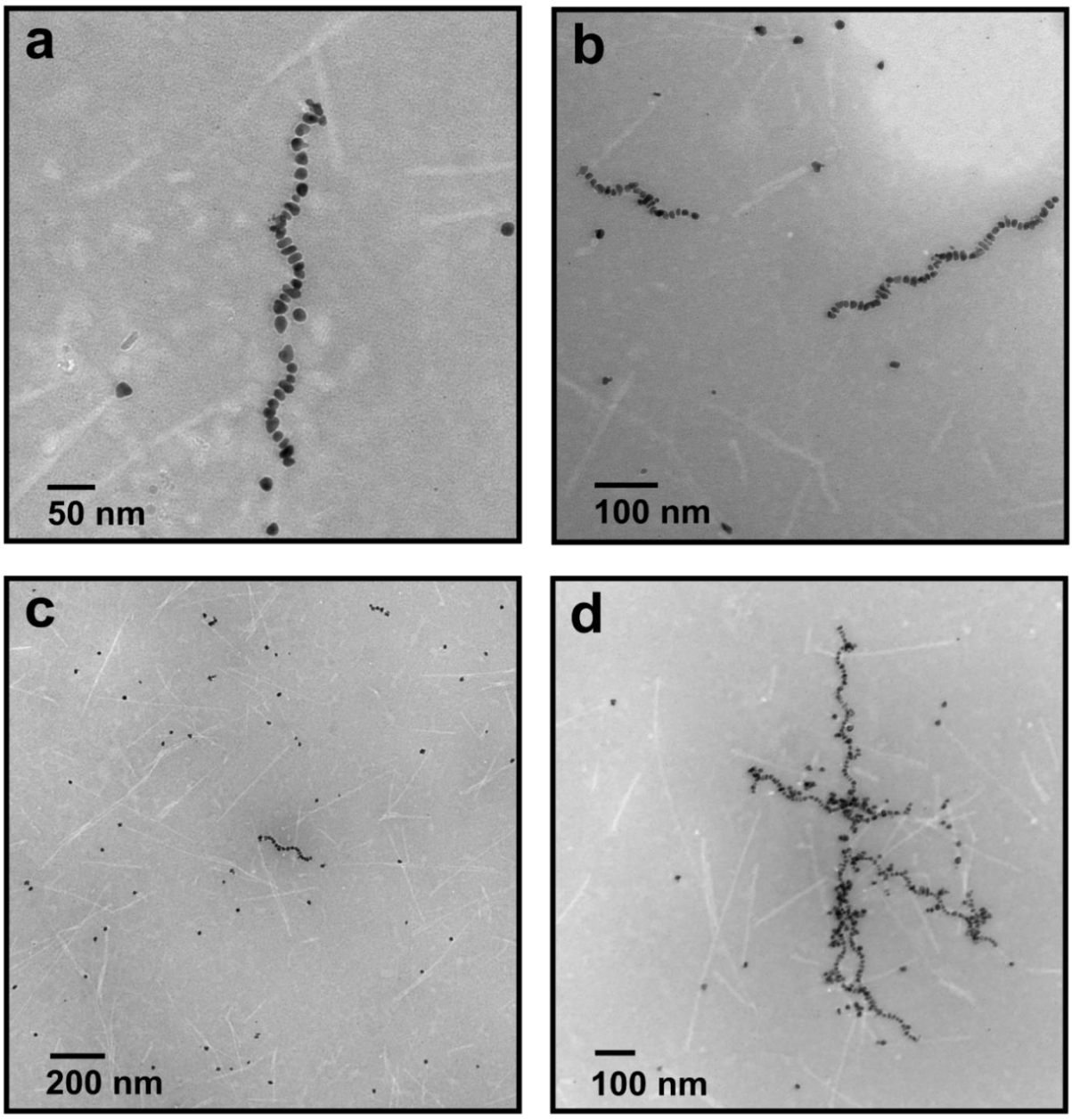

Appendix Figure 12. Negatively-stained TEM images of Au NP single helices formed using 10:10 C_{16}-$(PEP_{Au}^{M\text{-}ox})_2$: C_{16}-$(AYSSGA)_2$. These images, and others, were used for determining the fiber length distribution.

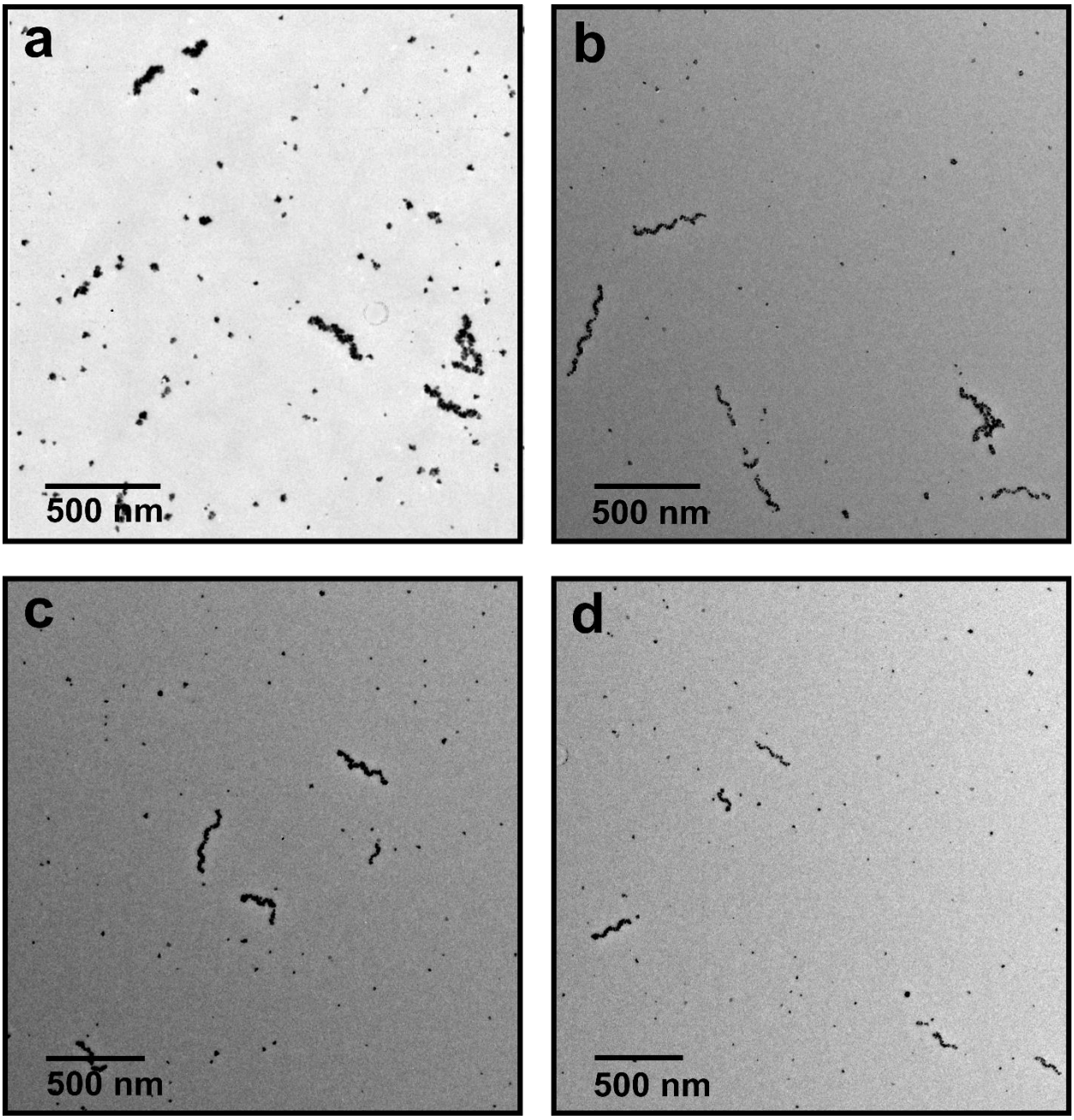

Appendix Figure 13. Additional TEM images of Au NP single helices formed using 10:15 C_{16}-$(PEP_{Au}^{M\text{-}ox})_2$: C_{16}-$(AYSSGA)_2$. These images, and others, were used for determining the helix length distribution.

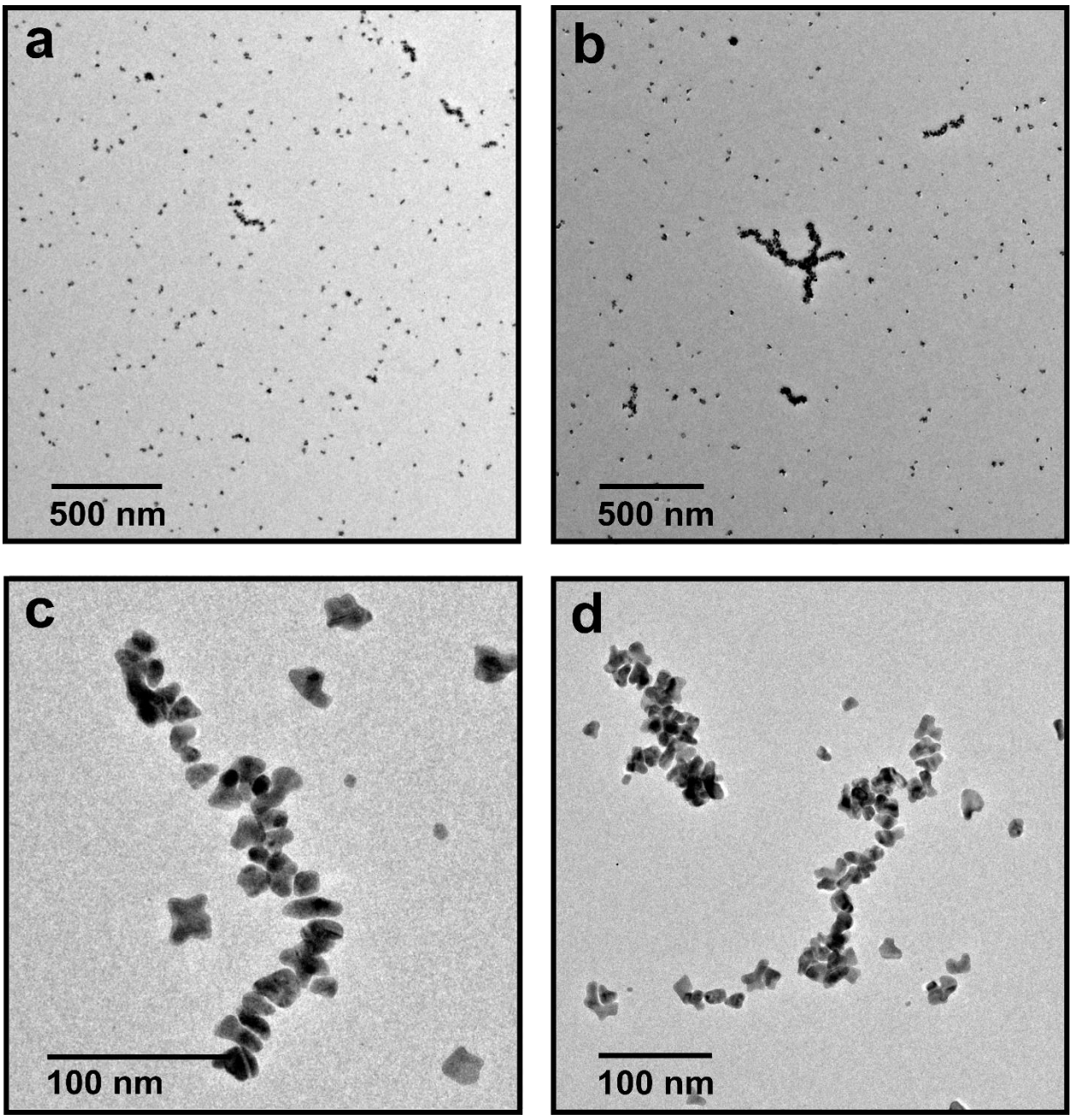

Appendix Figure 14. Representative TEM images of Au NP single helices formed using 10:25 C_{16}-$(PEP_{Au}^{M\text{-}ox})_2$ C_{16}-$(AYSSGA)_2$. These images, and others, were used for determining the helix length distribution.

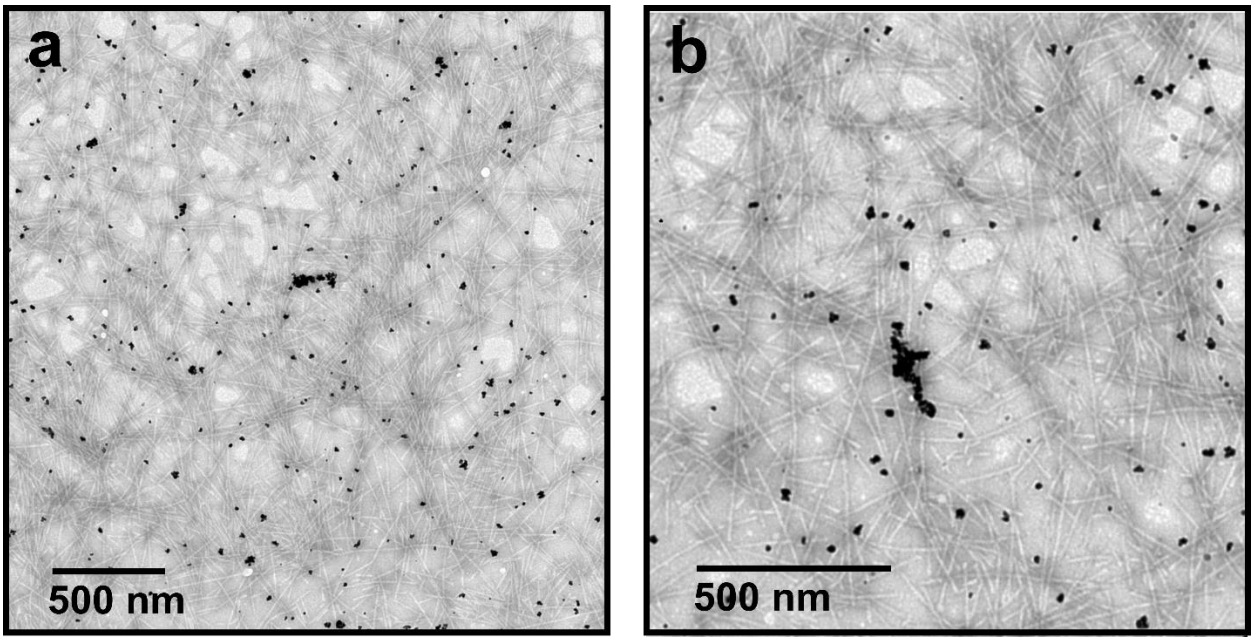

Appendix Figure 15 Negatively-stained TEM images of Au NP single helices formed using 10:25 C_{16}-$(PEP_{Au}^{M\text{-}ox})_2$: C_{16}-$(AYSSGA)_2$. These images, and others, were used for determining the fiber length distribution.

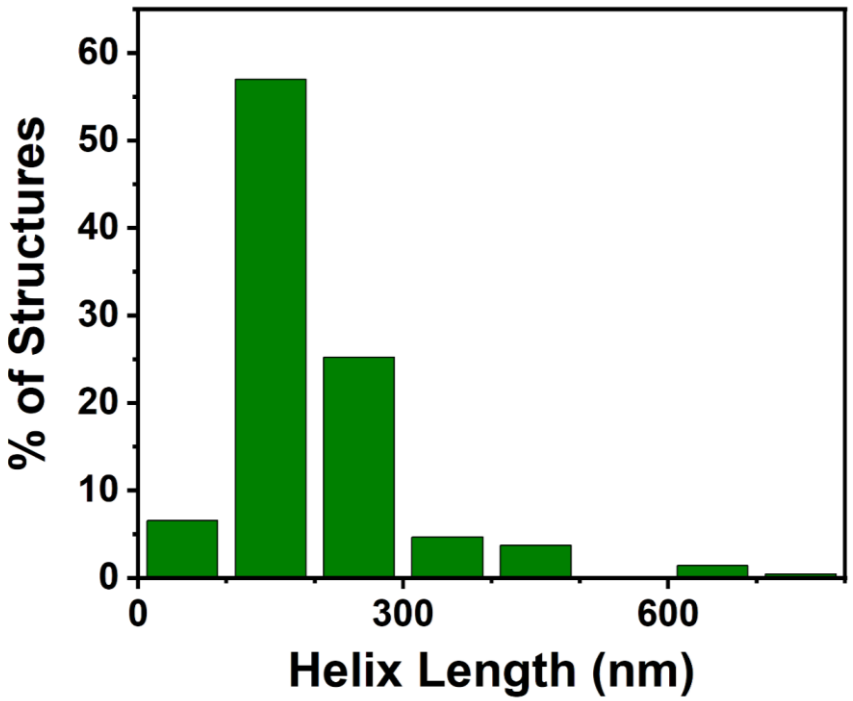

Appendix Figure 16 Helix length distribution of Au NP single helices formed using 10:25 C_{16}-$(PEP_{Au}^{M\text{-}ox})_2$: C_{16}-$(AYSSGA)_2$ (measurement based on 214 counts).

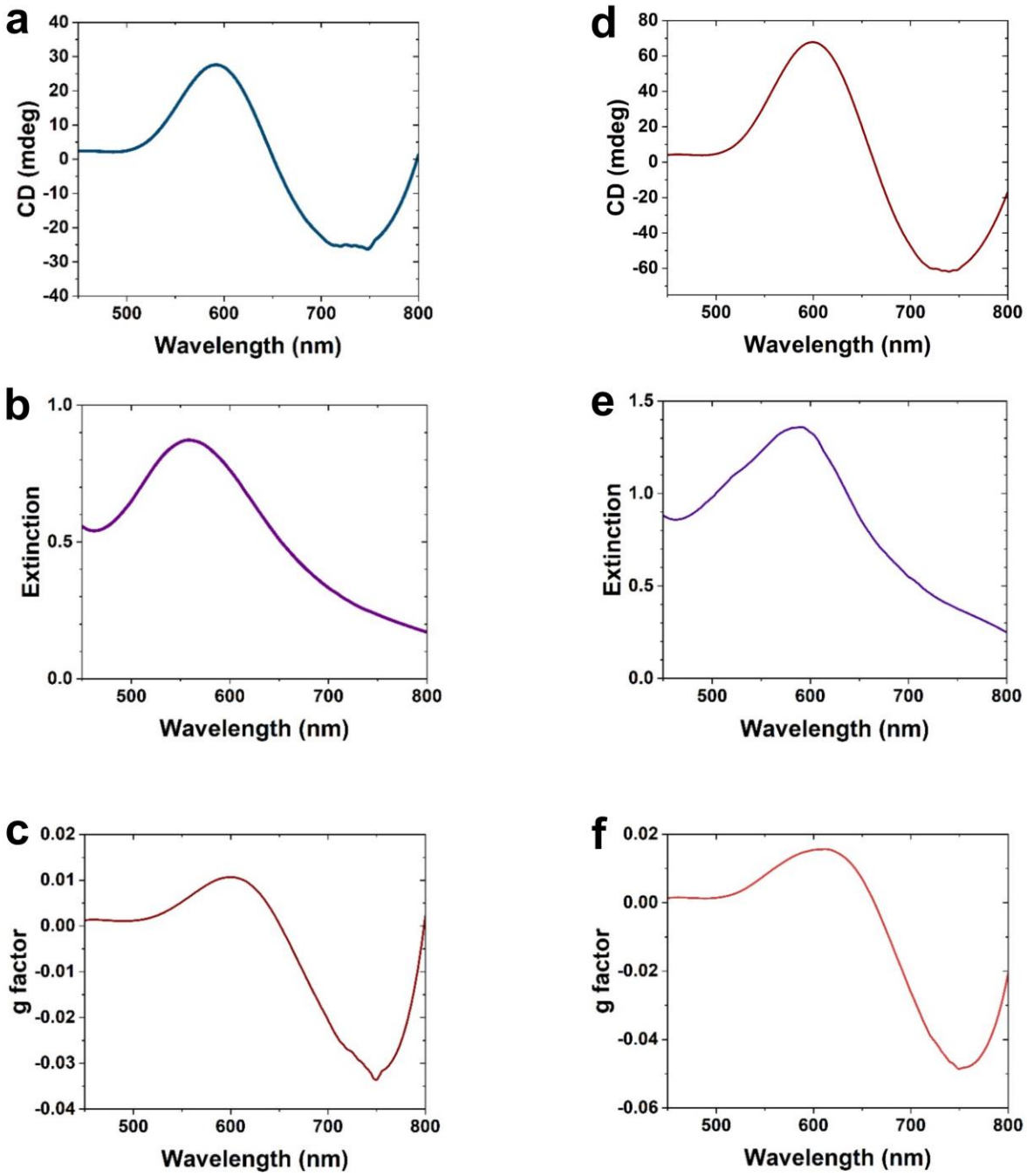

Appendix Figure 17 Plasmonic chiroptical activity of Au NP single helices formed using either 10:1 or 10:5 C_{16}-$(PEP_{Au}^{M\text{-}ox})_2$: C_{16}-$(AYSSGA)_2$. (a), (d) CD spectra of 10:1 and 10:5; (b), (e) UV-Vis spectra of 10:1 and 10:5; (c), (f) g factor plot of 10:1 and 10:5.

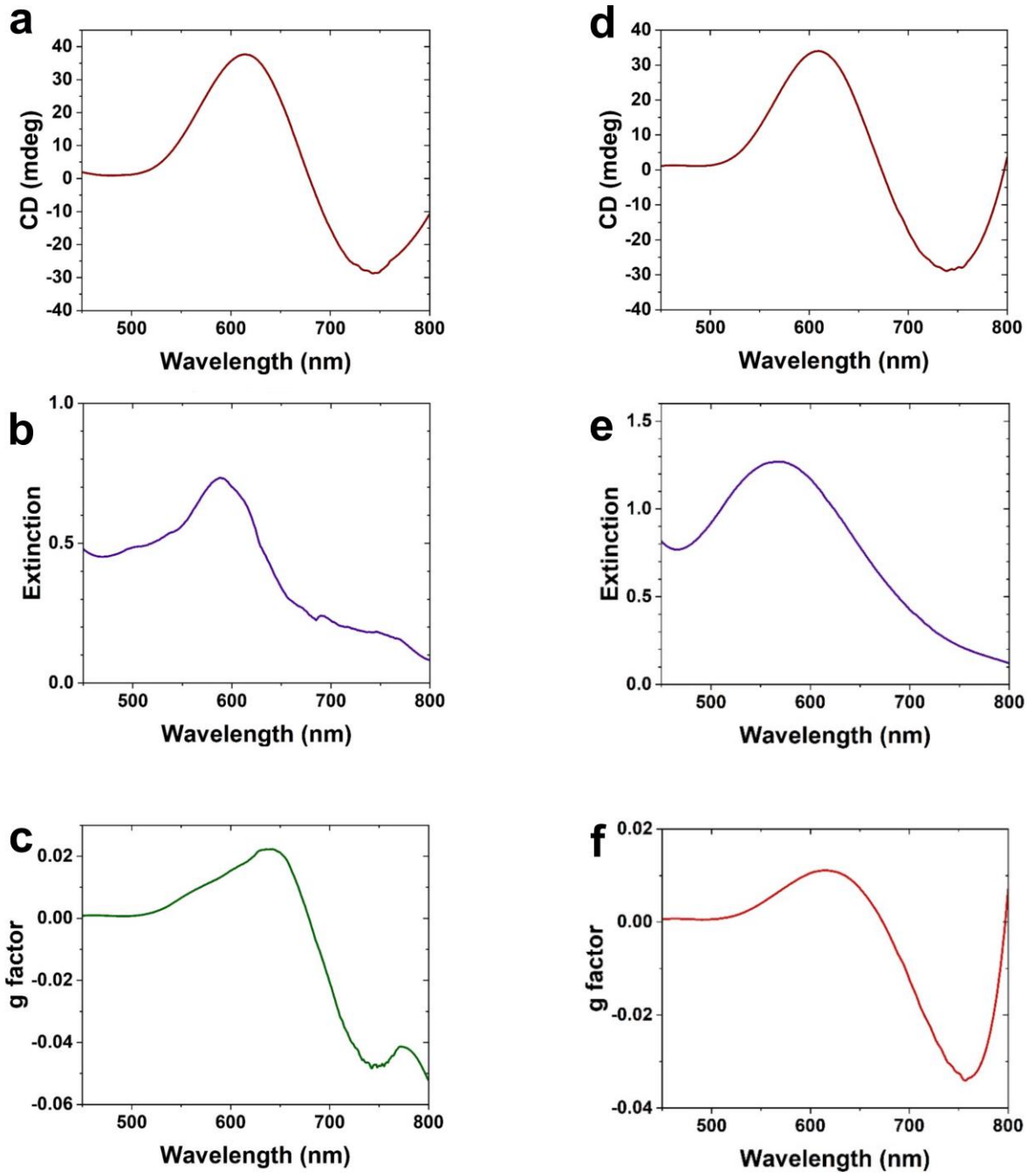

Appendix Figure 18 Plasmonic chiroptical activity of Au NP single helices formed using either 10:10 or 10:15 C_{16}-$(PEP_{Au}^{M\text{-}ox})_2$: C_{16}-$(AYSSGA)_2$. (a), (d) CD spectra of 10:10 and 10:15; (b), (e) UV-Vis spectra of 10:10 and 10:15; (c), (f) g factor plot of 10:10 and 10:15.

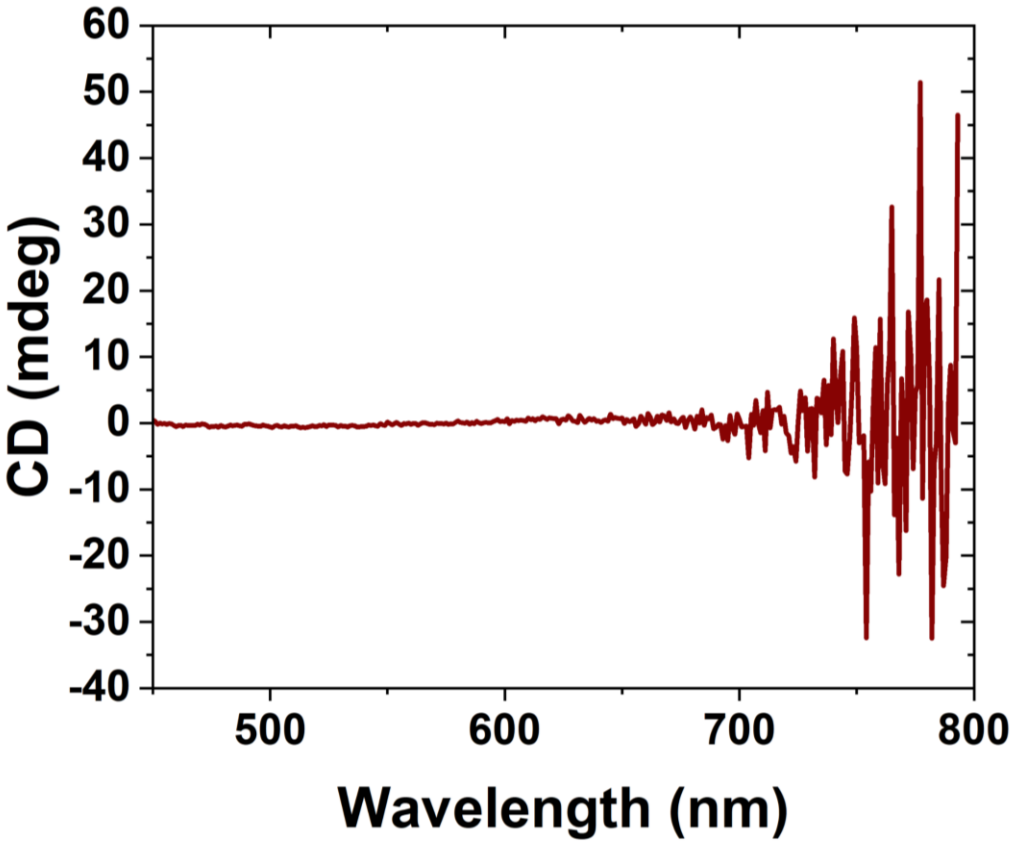

Appendix Figure 19 Plasmonic CD spectra of Au NP single helices formed using 10:25 C_{16}-$(PEP_{Au}^{M\text{-}ox})_2$: C_{16}-$(AYSSGA)_2$.

Sample	Pitch Length (nm)	Nanoparticle Width (nm)	Nanoparticle Length (nm)
10:1	83±12	9.4±1.6	16.4±3.1
10:5	82±12	10.0±2.0	21.1±4.7
10:10	81±10	11.3±2.6	19.3±5.1
10:15	84±12	11.3±1.9	17.3±2.9
10:25	94±18	10.8±2.4	20.9±4.2

Appendix Table 1 Structural parameters for single helices prepared using mixtures of C_{16}-$(PEP_{Au}^{M\text{-}ox})_2$ and C_{16}-$(AYSSGA)_2$. All measurement based on 100 counts.

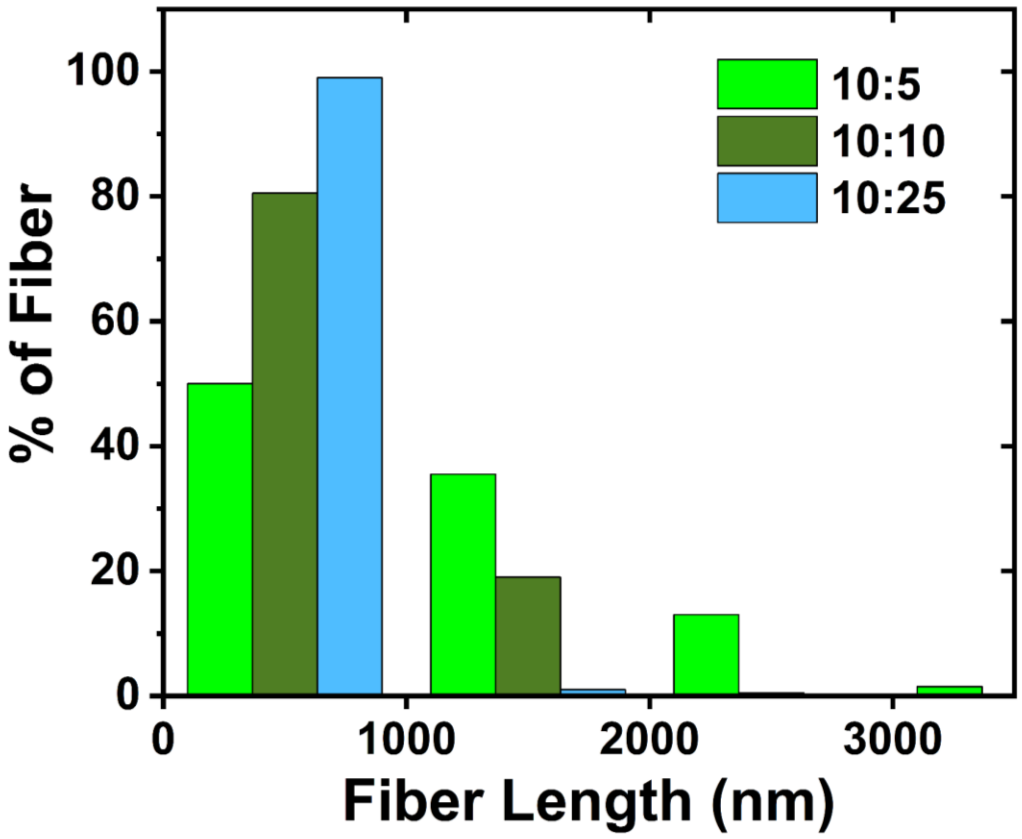

Appendix Figure 20. Length distributions of fibers prepared using mixtures of C_{16}-$(PEP_{Au}^{M\text{-}ox})_2$ and C_{16}-$(AYSSGA)_2$. Data based on measurements of fibers in Figures S10, S12, and S15.(150 counts for each condition).

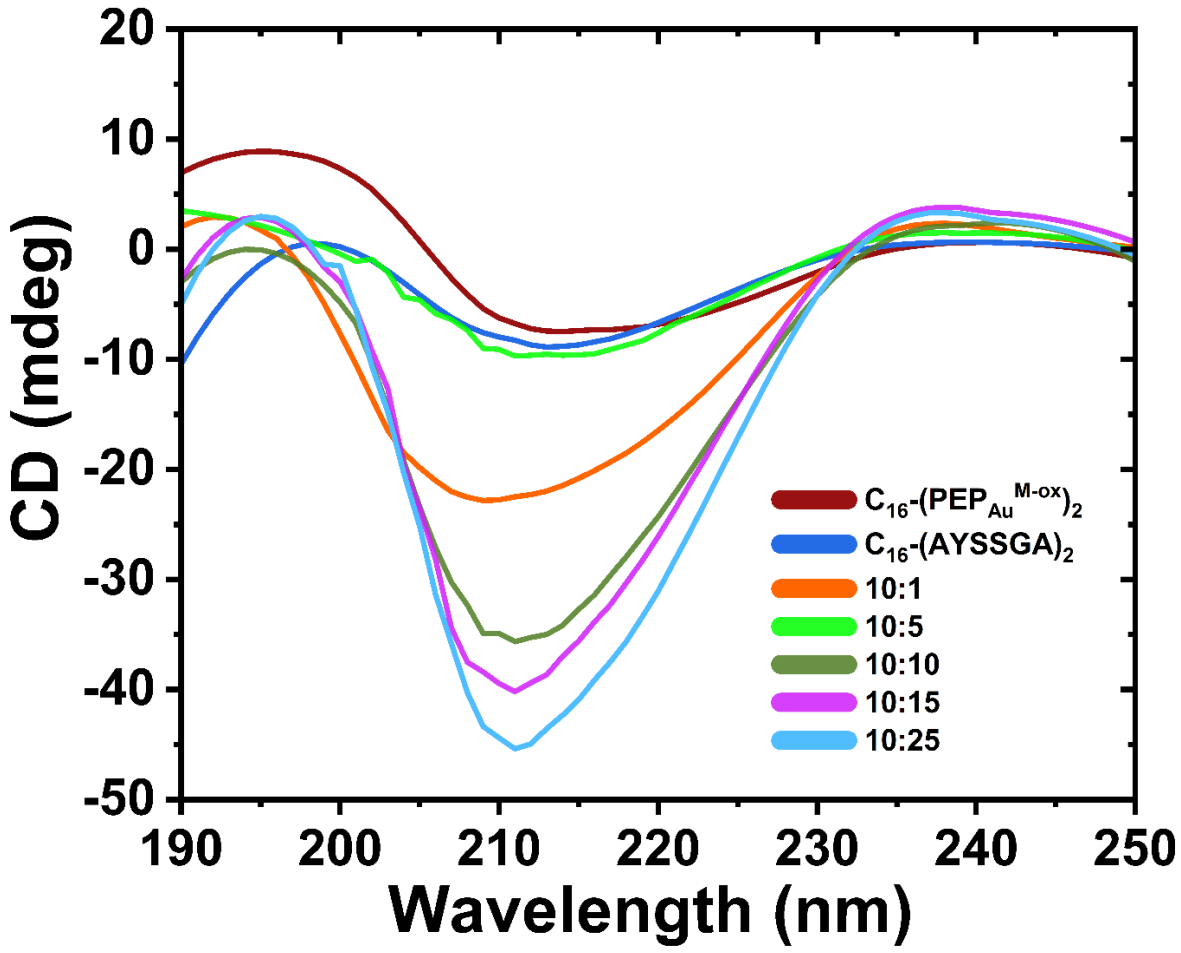

Appendix Figure 21. CD spectra of fibers prepared using mixtures of C_{16}-$(PEP_{Au}^{M\text{-}ox})_2$ and C_{16}-$(AYSSGA)_2$.

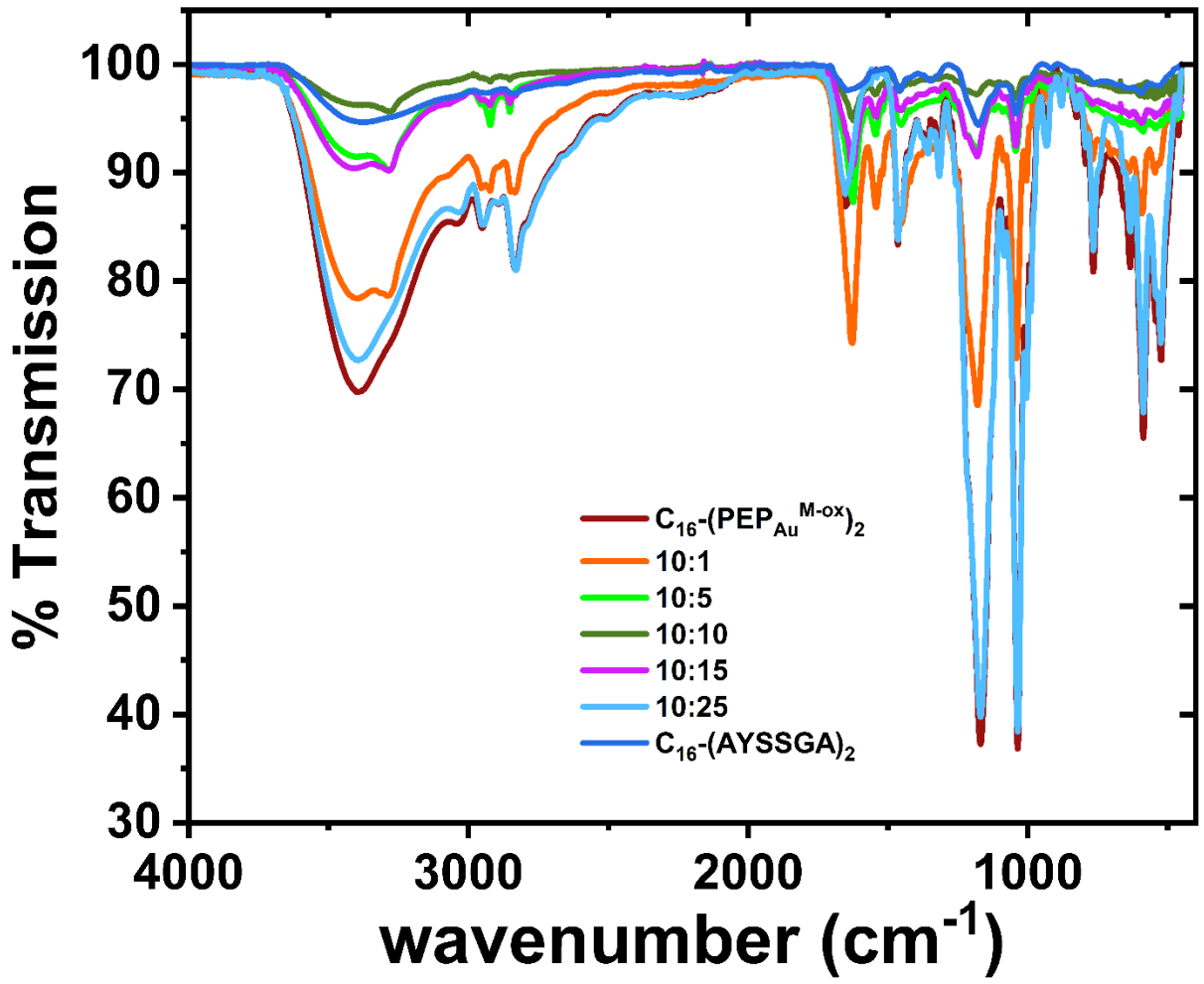

Appendix Figure 22. FTIR spectra of fibers prepared using mixtures of C_{16}-$(PEP_{Au}^{M\text{-}ox})_2$ and C_{16}-$(AYSSGA)_2$.

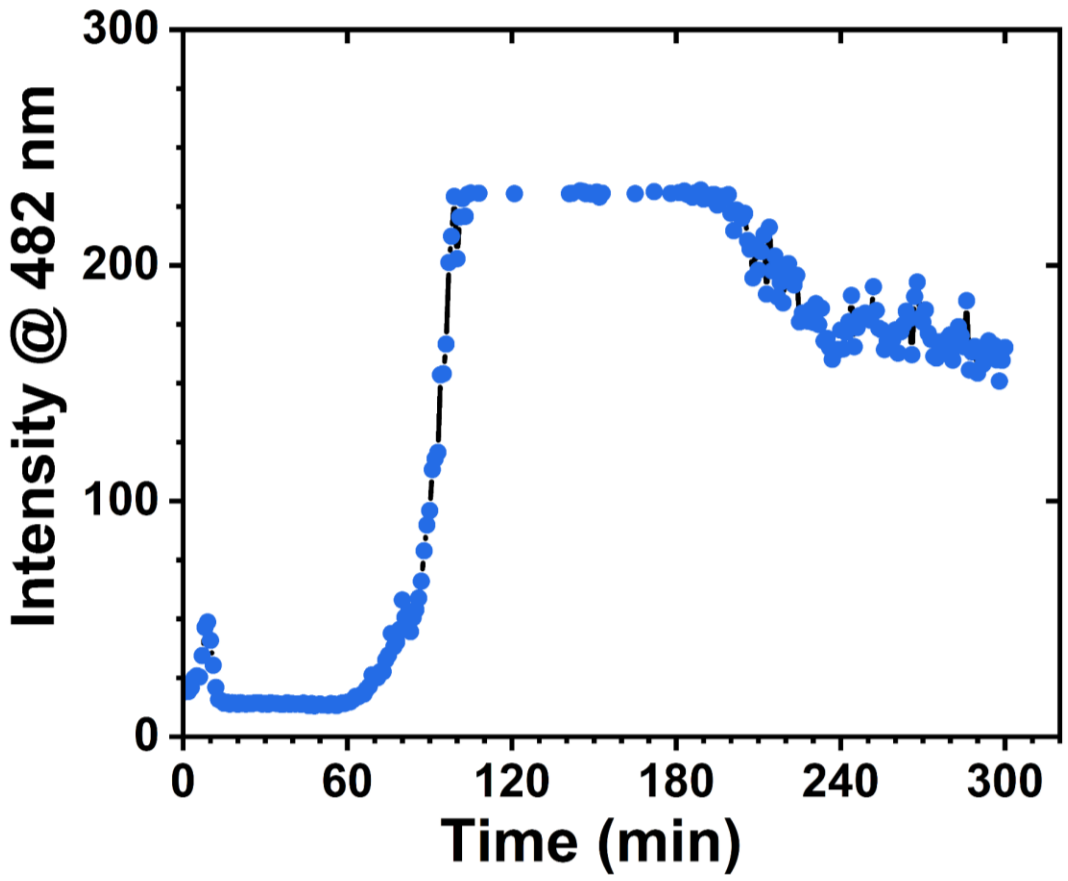

Appendix Figure 23. ThT fluorescence study of modulator assembly in 1:1 mixture of acetonitrile and H_2O.

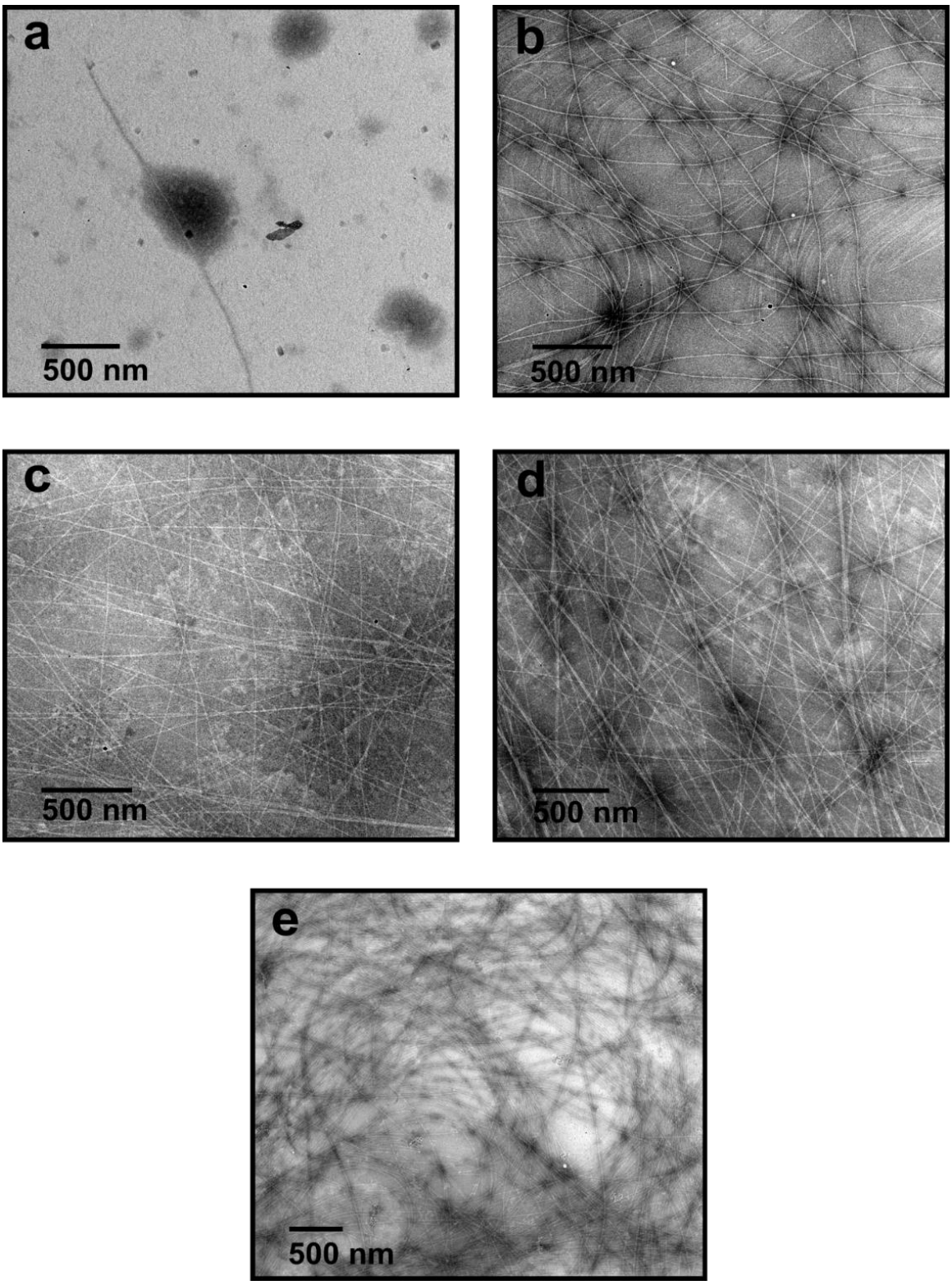

Appendix Figure 24. Negatively-stained TEM images of C_{16}-$(PEP_{Au}^{M\text{-}ox})_2$-based fibers at different assembly timepoints (a) 0 min, (b) 1 h, (c) 2 h, (d) 3h, and (e) 18h.

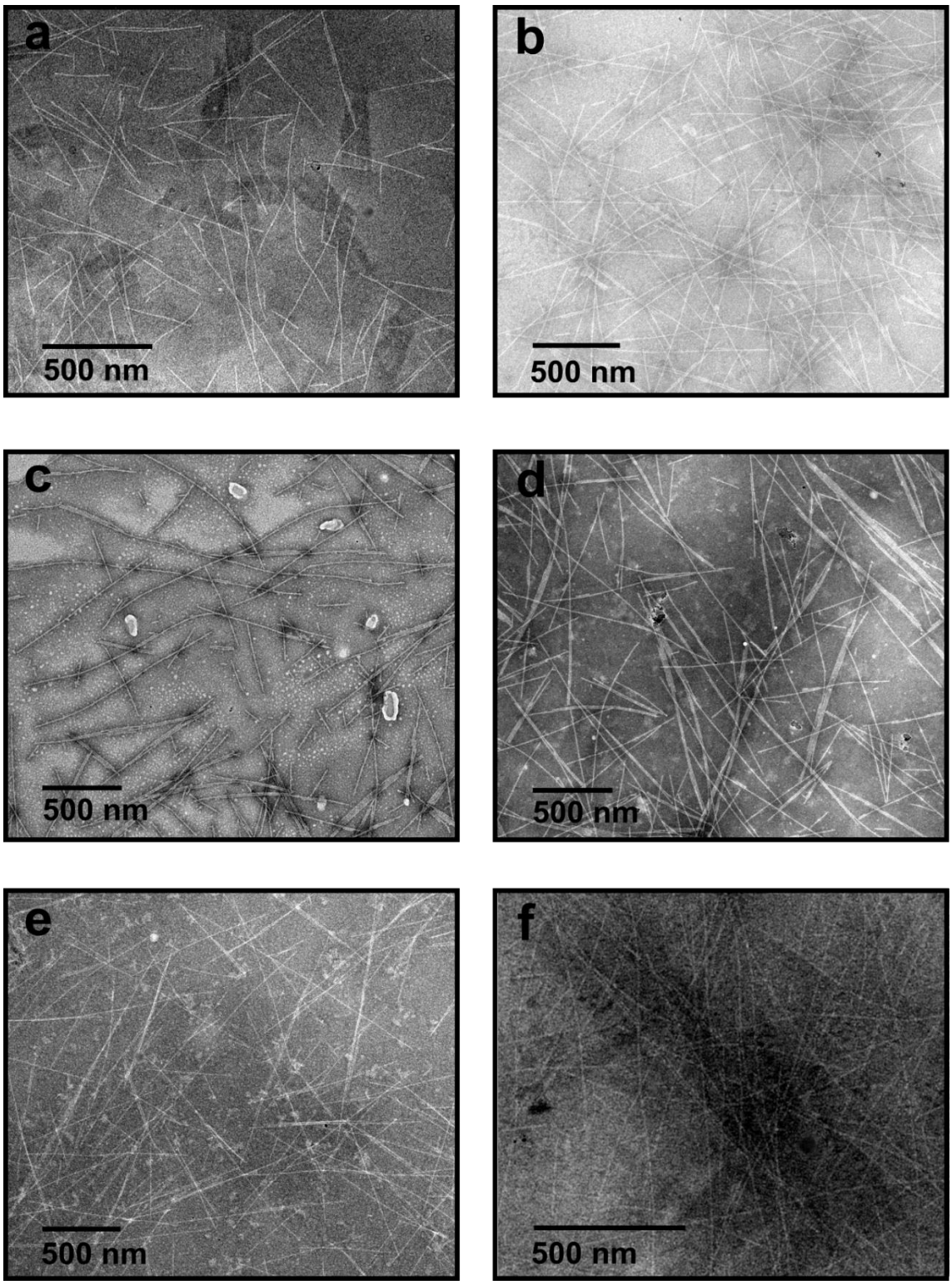

Appendix Figure 25. Negatively-stained TEM images of C_{16}-$(AYSSGA)_2$-based fibers at different assembly timepoints (a) 0 min, (b) 30 min, (c) 2 h, (d) 3 h, (e) 4 h, and (f) 18 h.

Time	Modulator Fiber Length		
	< 1000 nm	Median (nm)	Average (nm)
0 min	~93%	~447	~503
1 h	~93%	~400	~485
3 h	~58%	~910	~999
18 h	~50%	~993	~1119

Appendix Table 2.C_{16}-$(AYSSGA)_2$-based fiber lengths at different assembly timepoints (measurements based on 150 counts).

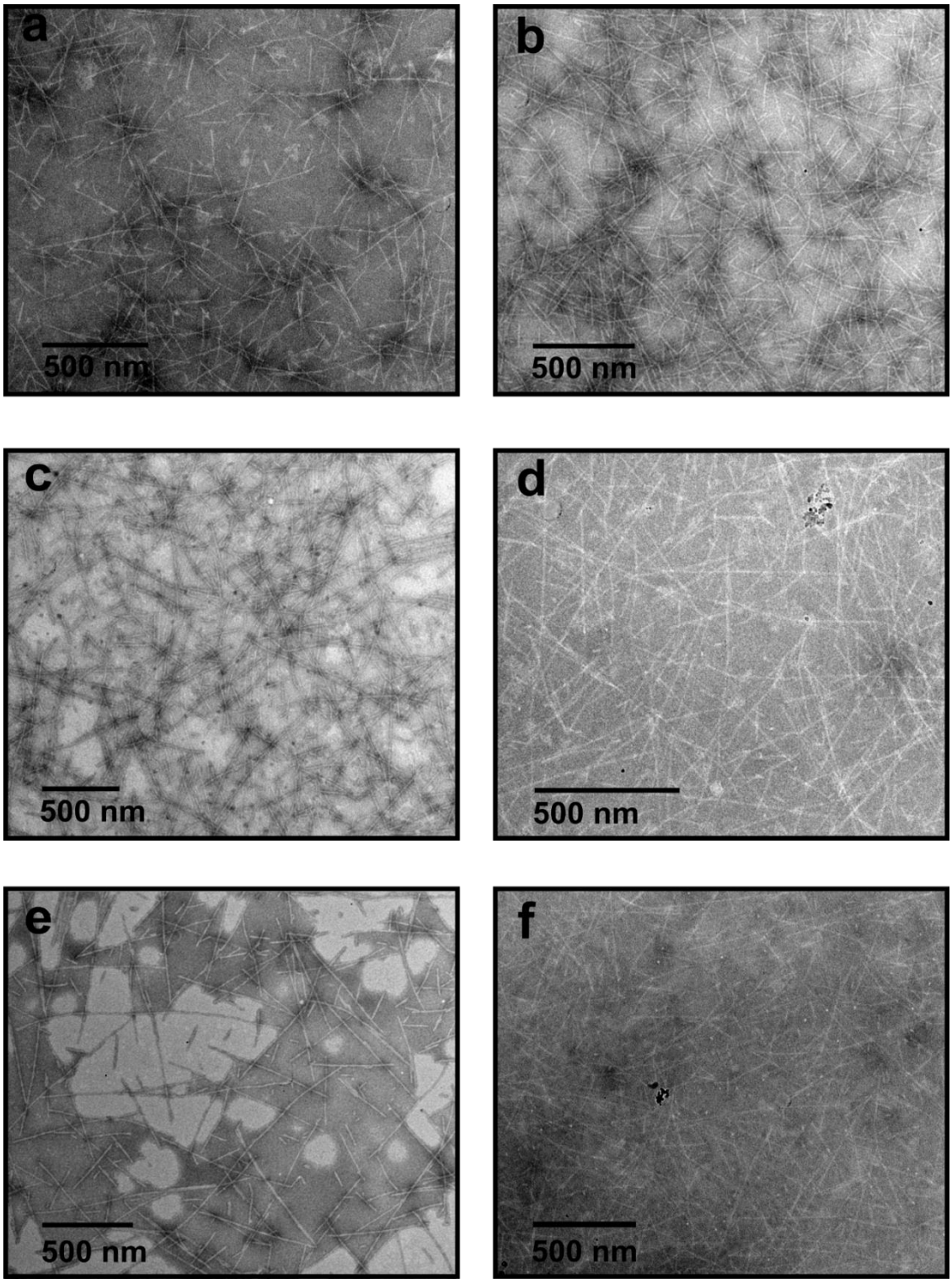

Appendix Figure 26. Negatively-stained TEM images of fibers formed from 10:10 C_{16}-$(PEP_{Au}^{M\text{-}ox})_2$: C_{16}-$(AYSSGA)_2$ at different assembly timepoint (a) 0 min, (b) 30 min, (c) 1 h, (d) 3 h, (e) 4 h, and (f) 18 h.

Time	"10:10" Fiber Length		
	< 1000 nm	Median (nm)	Average (nm)
0 min	~100%	~259	~293
30 min	~88%	~548	~601
4 h	~74%	~720	~926
18 h	~87%	~640	~677

Appendix Table 3. Lengths of fibers formed using 10:10 C_{16}-$(PEP_{Au}^{M\text{-}ox})_2$: C_{16}-$(AYSSGA)_2$ at different assembly timepoints (measurement based on 150 counts).

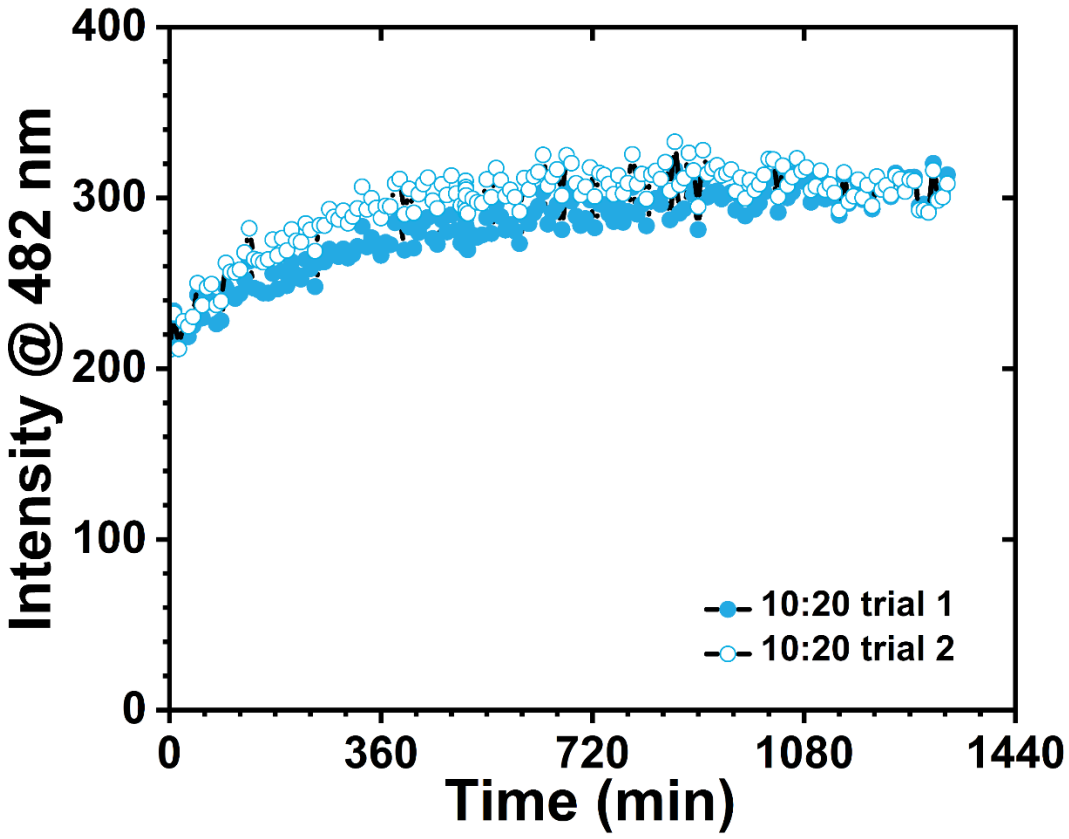

Appendix Figure 27.ThT fluorescence study of fiber assembly of 10:20 C_{16}-$(PEP_{Au}^{M\text{-}ox})_2$: C_{16}-$(AYSSGA)_2$

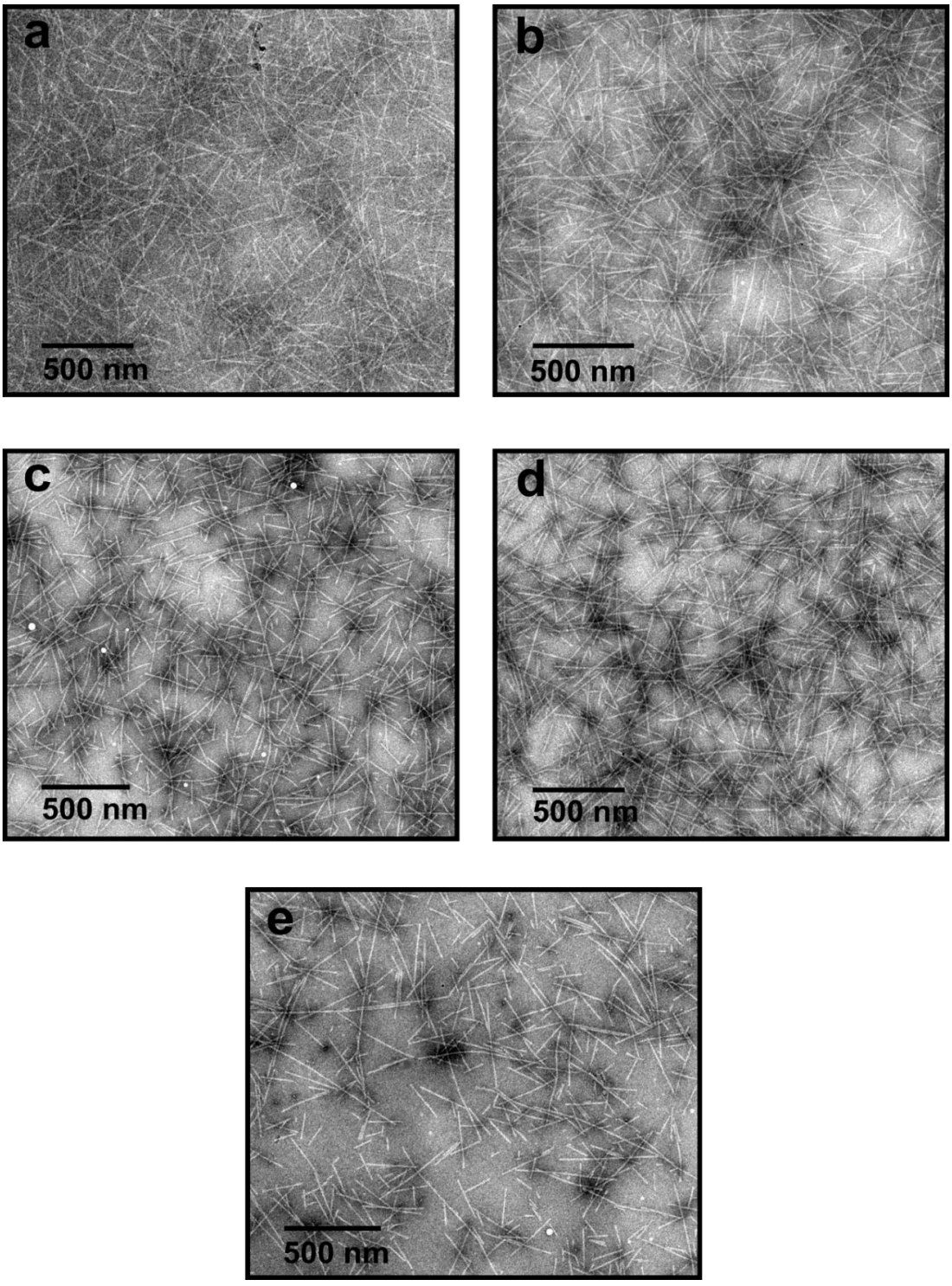

Appendix Figure 28Negatively-stained TEM images fibers formed using 10:20 C_{16}-$(PEP_{Au}^{M\text{-}ox})_2$: C_{16}-$(AYSSGA)_2$ at different assembly timepoints (a) 0 min, (b) 1 h, (c) 2 h, (d) 3 h, and (e) 48 h.

Time	"10:20" Fiber Length		
	< 1000 nm	Median (nm)	Average (nm)
0 min	~100%	~341	~388
1 h	~99%	~305	~329
3 h	~100%	~363	~390
48 h	~100%	~300	~335

Appendix Table 4. Lengths of fibers formed using 10:20 C_{16}-$(PEP_{Au}^{M\text{-}ox})_2$: C_{16}-$(AYSSGA)_2$ at different assembly timepoints (measurement based on 150 counts).

Bibliography

(1) Weiner, S.; Wagner, H. D. THE MATERIAL BONE: Structure-Mechanical Function Relations. *Annu. Rev. Mater. Sci.* **1998**, *28* (1), 271–298. https://doi.org/10.1146/annurev.matsci.28.1.271.

(2) Whitesides, G. M.; Grzybowski, B. Self-Assembly at All Scales. *Science* **2002**, *295* (5564), 2418–2421. https://doi.org/10.1126/science.1070821.

(3) Estroff, L. A. Introduction: Biomineralization. *Chem. Rev.* **2008**, *108* (11), 4329–4331. https://doi.org/10.1021/cr8004789.

(4) Yao, S.; Jin, B.; Liu, Z.; Shao, C.; Zhao, R.; Wang, X.; Tang, R. Biomineralization: From Material Tactics to Biological Strategy. *Advanced Materials* **2017**, *29* (14), 1605903. https://doi.org/10.1002/adma.201605903.

(5) Hartgerink, J. D.; Beniash, E.; Stupp, S. I. Self-Assembly and Mineralization of Peptide-Amphiphile Nanofibers. *Science* **2001**, *294* (5547), 1684–1688. https://doi.org/10.1126/science.1063187.

(6) Hendricks, M. P.; Sato, K.; Palmer, L. C.; Stupp, S. I. Supramolecular Assembly of Peptide Amphiphiles. *Acc. Chem. Res.* **2017**, *50* (10), 2440–2448. https://doi.org/10.1021/acs.accounts.7b00297.

(7) Hong, F.; Zhang, F.; Liu, Y.; Yan, H. DNA Origami: Scaffolds for Creating Higher Order Structures. *Chem. Rev.* **2017**, *117* (20), 12584–12640. https://doi.org/10.1021/acs.chemrev.6b00825.

(8) Wilner, O. I.; Willner, I. Functionalized DNA Nanostructures. *Chem. Rev.* **2012**, *112* (4), 2528–2556. https://doi.org/10.1021/cr200104q.

(9) Janairo, J.; Sakaguchi, T.; Mine, K.; Kamada, R.; Sakaguchi, K. Synergic Strategies for the Enhanced Self-Assembly of Biomineralization Peptides for the Synthesis of Functional Nanomaterials. *PROTEIN AND PEPTIDE LETTERS* **2018**, *25* (1), 4–14. https://doi.org/10.2174/0929866525666171214110206.

(10) Nudelman, F.; Sommerdijk, N. A. J. M. Biomineralization as an Inspiration for Materials Chemistry. *Angewandte Chemie International Edition* **2012**, *51* (27), 6582–6596. https://doi.org/10.1002/anie.201106715.

(11) Chen, C.-L.; Rosi, N. L. Peptide-Based Methods for the Preparation of Nanostructured Inorganic Materials. *Angewandte Chemie International Edition* **2010**, *49* (11), 1924–1942. https://doi.org/10.1002/anie.200903572.

(12) Lv, J.; Gao, X.; Han, B.; Zhu, Y.; Hou, K.; Tang, Z. Self-Assembled Inorganic Chiral Superstructures. *Nature Reviews Chemistry* **2022**, *6* (2), 125–145. https://doi.org/10.1038/s41570-021-00350-w.

(13) Ma, W.; Xu, L.; de Moura, A. F.; Wu, X.; Kuang, H.; Xu, C.; Kotov, N. A. Chiral Inorganic Nanostructures. *Chem. Rev.* **2017**, *117* (12), 8041–8093. https://doi.org/10.1021/acs.chemrev.6b00755.

(14) Pigliacelli, C.; Sánchez-Fernández, R.; García, M. D.; Peinador, C.; Pazos, E. Self-Assembled Peptide–Inorganic Nanoparticle Superstructures: From Component Design to Applications. *Chem. Commun.* **2020**, *56* (58), 8000–8014. https://doi.org/10.1039/D0CC02914A.

(15) Tang, Z.; Kotov, N. A. One-Dimensional Assemblies of Nanoparticles: Preparation, Properties, and Promise. *Advanced Materials* **2005**, *17* (8), 951–962. https://doi.org/10.1002/adma.200401593.

(16) Gao, Y.; Tang, Z. Design and Application of Inorganic Nanoparticle Superstructures: Current Status and Future Challenges. *Small* **2011**, *7* (15), 2133–2146. https://doi.org/10.1002/smll.201100474.

(17) Kotov, N. A.; Liz-Marzán, L. M.; Wang, Q. Chiral Nanomaterials: Evolving Rapidly from Concepts to Applications. *Mater. Adv.* **2022**, *3* (9), 3677–3679. https://doi.org/10.1039/D2MA90034C.

(18) Aida, T.; Meijer, E. W.; Stupp, S. I. Functional Supramolecular Polymers. *Science* **2012**, *335* (6070), 813–817. https://doi.org/10.1126/science.1205962.

(19) Choi, C. L.; Alivisatos, A. P. From Artificial Atoms to Nanocrystal Molecules: Preparation and Properties of More Complex Nanostructures. *Annu. Rev. Phys. Chem.* **2010**, *61* (1), 369–389. https://doi.org/10.1146/annurev.physchem.012809.103311.

(20) De Santis, E.; Ryadnov, M. G. Peptide Self-Assembly for Nanomaterials: The Old New Kid on the Block. *Chem. Soc. Rev.* **2015**, *44* (22), 8288–8300. https://doi.org/10.1039/C5CS00470E.

(21) Zhang, Z.; Zhu, W.; Kodadek, T. Selection and Application of Peptide-Binding Peptides. *Nature Biotechnology* **2000**, *18* (1), 71–74. https://doi.org/10.1038/71951.

(22) Ulijn, R. V.; Smith, A. M. Designing Peptide Based Nanomaterials. *Chem. Soc. Rev.* **2008**, *37* (4), 664–675. https://doi.org/10.1039/B609047H.

(23) Chen, C.-L.; Zhang, P.; Rosi, N. L. A New Peptide-Based Method for the Design and Synthesis of Nanoparticle Superstructures: Construction of Highly Ordered Gold Nanoparticle Double Helices. *J. Am. Chem. Soc.* **2008**, *130* (41), 13555–13557. https://doi.org/10.1021/ja805683r.

(24) Walsh, T. R.; Knecht, M. R. Biointerface Structural Effects on the Properties and Applications of Bioinspired Peptide-Based Nanomaterials. *Chem. Rev.* **2017**, *117* (20), 12641–12704. https://doi.org/10.1021/acs.chemrev.7b00139.

(25) Seeman, N. C.; Belcher, A. M. Emulating Biology: Building Nanostructures from the Bottom Up. *Proceedings of the National Academy of Sciences* **2002**, *99* (suppl_2), 6451–6455. https://doi.org/10.1073/pnas.221458298.

(26) Flynn, C. E.; Mao, C.; Hayhurst, A.; Williams, J. L.; Georgiou, G.; Iverson, B.; Belcher, A. M. Synthesis and Organization of Nanoscale II–VI Semiconductor Materials Using Evolved Peptide Specificity and Viral Capsid Assembly. *J. Mater. Chem.* **2003**, *13* (10), 2414–2421. https://doi.org/10.1039/B307593A.

(27) Song, C.; Blaber, M. G.; Zhao, G.; Zhang, P.; Fry, H. C.; Schatz, G. C.; Rosi, N. L. Tailorable Plasmonic Circular Dichroism Properties of Helical Nanoparticle Superstructures. *Nano Lett.* **2013**, *13*, 3256.

(28) Merg, A. D.; Boatz, J. C.; Mandal, A.; Zhao, G.; Mokashi-Punekar, S.; Liu, C.; Wang, X.; Zhang, P.; van der Wel, P. C. A.; Rosi, N. L. Peptide-Directed Assembly of Single-Helical Gold Nanoparticle Superstructures Exhibiting Intense Chiroptical Activity. *J. Am. Chem. Soc.* **2016**, *138* (41), 13655–13663. https://doi.org/10.1021/jacs.6b07322.

(29) Song, C.; Zhao, G.; Zhang, P.; Rosi, N. L. Expeditious Synthesis and Assembly of Sub-100 Nm Hollow Spherical Gold Nanoparticle Superstructures. *J. Am. Chem. Soc.* **2010**, *132* (40), 14033–14035. https://doi.org/10.1021/ja106833g.

(30) Hwang, L.; Chen, C.-L.; Rosi, N. L. Preparation of 1-D Nanoparticle Superstructures with Tailorable Thicknesses Using Gold-Binding Peptide Conjugates. *Chem. Commun.* **2011**, *47* (1), 185–187. https://doi.org/10.1039/C0CC02257H.

(31) Merg, A. D.; Slocik, J.; Blaber, M. G.; Schatz, G. C.; Naik, R.; Rosi, N. L. Adjusting the Metrics of 1-D Helical Gold Nanoparticle Superstructures Using Multivalent Peptide Conjugates. *Langmuir* **2015**, *31* (34), 9492–9501. https://doi.org/10.1021/acs.langmuir.5b02208.

(32) Brooks, S. C.; Jin, R.; Zerbach, V. C.; Zhang, Y.; Walsh, T. R.; Rosi, N. L. Single Amino Acid Modifications for Controlling the Helicity of Peptide-Based Chiral Gold Nanoparticle Superstructures. *J. Am. Chem. Soc.* **2023**, *145* (11), 6546–6553. https://doi.org/10.1021/jacs.3c00827.

(33) Mokashi-Punekar, S.; Merg, A. D.; Rosi, N. L. Systematic Adjustment of Pitch and Particle Dimensions within a Family of Chiral Plasmonic Gold Nanoparticle Single Helices. *J. Am. Chem. Soc.* **2017**, *139* (42), 15043–15048. https://doi.org/10.1021/jacs.7b07143.

(34) Mokashi-Punekar, S.; Walsh, T. R.; Rosi, N. L. Tuning the Structure and Chiroptical Properties of Gold Nanoparticle Single Helices via Peptide Sequence Variation. *J. Am. Chem. Soc.* **2019**, *141* (39), 15710–15716. https://doi.org/10.1021/jacs.9b08798.

(35) Nie, Z.; Petukhova, A.; Kumacheva, E. Properties and Emerging Applications of Self-Assembled Structures Made from Inorganic Nanoparticles. *Nature Nanotechnology* **2010**, *5* (1), 15–25. https://doi.org/10.1038/nnano.2009.453.

(36) Jones, M. R.; Osberg, K. D.; Macfarlane, R. J.; Langille, M. R.; Mirkin, C. A. Templated Techniques for the Synthesis and Assembly of Plasmonic Nanostructures. *Chem. Rev.* **2011**, *111* (6), 3736–3827. https://doi.org/10.1021/cr1004452.

(37) Mokashi-Punekar, S.; Zhou, Y.; Brooks, S. C.; Rosi, N. L. Construction of Chiral, Helical Nanoparticle Superstructures: Progress and Prospects. *Advanced Materials* **2020**, *32* (41), 1905975. https://doi.org/10.1002/adma.201905975.

(38) Fan, Z.; Govorov, A. O. Helical Metal Nanoparticle Assemblies with Defects: Plasmonic Chirality and Circular Dichroism. *J. Phys. Chem. C* **2011**, *115* (27), 13254–13261. https://doi.org/10.1021/jp204265x.

(39) Hwang, L.; Zhao, G.; Zhang, P.; Rosi, N. L. Size-Controlled Peptide-Directed Synthesis of Hollow Spherical Gold Nanoparticle Superstructures. *Small* **2011**, *7* (14), 1939–1942. https://doi.org/10.1002/smll.201100477.

(40) Zhang, C.; Zhou, Y.; Merg, A.; Song, C.; Schatz, G. C.; Rosi, N. L. Hollow Spherical Gold Nanoparticle Superstructures with Tunable Diameters and Visible to Near-Infrared Extinction. *Nanoscale* **2014**, *6* (21), 12328–12332. https://doi.org/10.1039/C4NR04289A.

(41) Zhang, C.; Song, C.; Fry, H. C.; Rosi, N. L. Peptide Conjugates for Directing the Morphology and Assembly of 1D Nanoparticle Superstructures. *Chemistry – A European Journal* **2014**, *20* (4), 941–945. https://doi.org/10.1002/chem.201304074.

(42) Chen, C.-L.; Rosi, N. L. Preparation of Unique 1-D Nanoparticle Superstructures and Tailoring Their Structural Features. *J. Am. Chem. Soc.* **2010**, *132* (20), 6902–6903. https://doi.org/10.1021/ja102000g.

(43) Mokashi-Punekar, S.; Rosi, N. L. Deliberate Introduction of Particle Anisotropy in Helical Gold Nanoparticle Superstructures. *Particle & Particle Systems Characterization* **2019**, *36* (5), 1800504. https://doi.org/10.1002/ppsc.201800504.

(44) Mokashi-Punekar, S.; Brooks, S. C.; Hogan, C. D.; Rosi, N. L. Leveraging Peptide Sequence Modification to Promote Assembly of Chiral Helical Gold Nanoparticle Superstructures. *Biochemistry* **2021**, *60* (13), 1044–1049. https://doi.org/10.1021/acs.biochem.0c00361.

(45) Ke, W.; Lu, N.; Japir, A. A.-W. M. M.; Zhou, Q.; Xi, L.; Wang, Y.; Dutta, D.; Zhou, M.; Pan, Y.; Ge, Z. Length Effect of Stimuli-Responsive Block Copolymer Prodrug Filomicelles on Drug Delivery Efficiency. *Journal of Controlled Release* **2020**, *318*, 67–77. https://doi.org/10.1016/j.jconrel.2019.12.012.

(46) Jia, Z.; Bobrin, V. A.; Truong, N. P.; Gillard, M.; Monteiro, M. J. Multifunctional Nanoworms and Nanorods through a One-Step Aqueous Dispersion Polymerization. *J. Am. Chem. Soc.* **2014**, *136* (16), 5824–5827. https://doi.org/10.1021/ja500092m.

(47) Wang Xiaosong; Guerin Gerald; Wang Hai; Wang Yishan; Manners Ian; Winnik Mitchell A. Cylindrical Block Copolymer Micelles and Co-Micelles of Controlled Length and Architecture. *Science* **2007**, *317* (5838), 644–647. https://doi.org/10.1126/science.1141382.

(48) Geng, Y.; Dalhaimer, P.; Cai, S.; Tsai, R.; Tewari, M.; Minko, T.; Discher, D. E. Shape Effects of Filaments versus Spherical Particles in Flow and Drug Delivery. *Nature Nanotechnology* **2007**, *2* (4), 249–255. https://doi.org/10.1038/nnano.2007.70.

(49) Fries, C. N.; Wu, Y.; Kelly, S. H.; Wolf, M.; Votaw, N. L.; Zauscher, S.; Collier, J. H. Controlled Lengthwise Assembly of Helical Peptide Nanofibers to Modulate CD8+ T-Cell Responses. *Advanced Materials* **2020**, *32* (39), 2003310. https://doi.org/10.1002/adma.202003310.

(50) Whitehead, T. A.; Meadows, A. L.; Clark, D. S. Controlling the Self-Assembly of a Filamentous Hyperthermophilic Chaperone by an Engineered Capping Protein. *Small* **2008**, *4* (7), 956–960. https://doi.org/10.1002/smll.200700848.

(51) Adler-Abramovich, L.; Marco, P.; Arnon, Z. A.; Creasey, R. C. G.; Michaels, T. C. T.; Levin, A.; Scurr, D. J.; Roberts, C. J.; Knowles, T. P. J.; Tendler, S. J. B.; Gazit, E. Controlling the Physical Dimensions of Peptide Nanotubes by Supramolecular Polymer Coassembly. *ACS Nano* **2016**, *10* (8), 7436–7442. https://doi.org/10.1021/acsnano.6b01587.

(52) Besenius, P. Controlling Supramolecular Polymerization through Multicomponent Self-Assembly. *Journal of Polymer Science Part A: Polymer Chemistry* **2017**, *55* (1), 34–78. https://doi.org/10.1002/pola.28385.

(53) Tao, D.; Feng, C.; Cui, Y.; Yang, X.; Manners, I.; Winnik, M. A.; Huang, X. Monodisperse Fiber-like Micelles of Controlled Length and Composition with an Oligo(p-Phenylenevinylene) Core via "Living" Crystallization-Driven Self-Assembly. *J. Am. Chem. Soc.* **2017**, *139* (21), 7136–7139. https://doi.org/10.1021/jacs.7b02208.

(54) Qian, J.; Guerin, G.; Lu, Y.; Cambridge, G.; Manners, I.; Winnik, M. A. Self-Seeding in One Dimension: An Approach To Control the Length of Fiberlike Polyisoprene–Polyferrocenylsilane Block Copolymer Micelles. *Angewandte Chemie International Edition* **2011**, *50* (7), 1622–1625. https://doi.org/10.1002/anie.201006223.

(55) Qian, J.; Lu, Y.; Chia, A.; Zhang, M.; Rupar, P. A.; Gunari, N.; Walker, G. C.; Cambridge, G.; He, F.; Guerin, G.; Manners, I.; Winnik, M. A. Self-Seeding in One Dimension: A Route to Uniform Fiber-like Nanostructures from Block Copolymers with a Crystallizable Core-Forming Block. *ACS Nano* **2013**, *7* (5), 3754–3766. https://doi.org/10.1021/nn400124x.

(56) Patra, S. K.; Ahmed, R.; Whittell, G. R.; Lunn, D. J.; Dunphy, E. L.; Winnik, M. A.; Manners, I. Cylindrical Micelles of Controlled Length with a π-Conjugated Polythiophene Core via Crystallization-Driven Self-Assembly. *J. Am. Chem. Soc.* **2011**, *133* (23), 8842–8845. https://doi.org/10.1021/ja202408w.

(57) Song, Y.; Moore, E. G.; Guo, Y.; Moore, J. S. Polymer–Peptide Conjugates Disassemble Amyloid β Fibrils in a Molecular-Weight Dependent Manner. *J. Am. Chem. Soc.* **2017**, *139* (12), 4298–4301. https://doi.org/10.1021/jacs.7b00289.

(58) Pal, A.; Malakoutikhah, M.; Leonetti, G.; Tezcan, M.; Colomb-Delsuc, M.; Nguyen, V. D.; van der Gucht, J.; Otto, S. Controlling the Structure and Length of Self-Synthesizing Supramolecular Polymers through Nucleated Growth and Disassembly. *Angewandte Chemie International Edition* **2015**, *54* (27), 7852–7856. https://doi.org/10.1002/anie.201501965.

(59) Moyer, T. J.; Cui, H.; Stupp, S. I. Tuning Nanostructure Dimensions with Supramolecular Twisting. *J. Phys. Chem. B* **2013**, *117* (16), 4604–4610. https://doi.org/10.1021/jp3087978.

(60) Paramonov, S. E.; Jun, H.-W.; Hartgerink, J. D. Self-Assembly of Peptide−Amphiphile Nanofibers: The Roles of Hydrogen Bonding and Amphiphilic Packing. *J. Am. Chem. Soc.* **2006**, *128* (22), 7291–7298. https://doi.org/10.1021/ja060573x.

(61) Adochitei, A.; Drochioiu, G. Rapid Characterization of Peptide Secondary Structure by FT-IR Spectroscopy. *Revue Roumaine de Chimie* **2011**, *56*, 783–791.

(62) Yang, H.; Yang, S.; Kong, J.; Dong, A.; Yu, S. Obtaining Information about Protein Secondary Structures in Aqueous Solution Using Fourier Transform IR Spectroscopy. *Nature Protocols* **2015**, *10* (3), 382–396. https://doi.org/10.1038/nprot.2015.024.

(63) Jiang, H.; Guler, M. O.; Stupp, S. I. The Internal Structure of Self-Assembled Peptide Amphiphiles Nanofibers. *Soft Matter* **2007**, *3* (4), 454–462. https://doi.org/10.1039/B614426H.

(64) Hudson, S. A.; Ecroyd, H.; Kee, T. W.; Carver, J. A. The Thioflavin T Fluorescence Assay for Amyloid Fibril Detection Can Be Biased by the Presence of Exogenous Compounds. *The FEBS Journal* **2009**, *276* (20), 5960–5972. https://doi.org/10.1111/j.1742-4658.2009.07307.x.

(65) Xue, C.; Lin, T. Y.; Chang, D.; Guo, Z. Thioflavin T as an Amyloid Dye: Fibril Quantification, Optimal Concentration and Effect on Aggregation. *Royal Society Open Science 4* (1), 160696. https://doi.org/10.1098/rsos.160696.

(66) Hartlieb, M.; Mansfield, E. D. H.; Perrier, S. A Guide to Supramolecular Polymerizations. *Polym. Chem.* **2020**, *11* (6), 1083–1110. https://doi.org/10.1039/C9PY01342C.

(67) Schindelin, J.; Arganda-Carreras, I.; Frise, E.; Kaynig, V.; Longair, M.; Pietzsch, T.; Preibisch, S.; Rueden, C.; Saalfeld, S.; Schmid, B.; Tinevez, J.-Y.; White, D. J.; Hartenstein, V.; Eliceiri, K.; Tomancak, P.; Cardona, A. Fiji: An Open-Source Platform

for Biological-Image Analysis. *Nature Methods* **2012**, *9* (7), 676–682. https://doi.org/10.1038/nmeth.2019.

(68) Schneider, C. A.; Rasband, W. S.; Eliceiri, K. W. NIH Image to ImageJ: 25 Years of Image Analysis. *Nature Methods* **2012**, *9* (7), 671–675. https://doi.org/10.1038/nmeth.2089.